J Adv Ceram

Research Article

Revealing corrosion mechanisms and enabling predictive lifetime assessment of high-entropy rare-earth disilicates with superior CMAS corrosion resistance

Yun Fan[1,2], Yuelei Bai[1,✉], Xiaodong He[1], Dong Chen[3], Zhaoxu Sun[1], Zhiyao Lu[1], Yuchen Liu[4], Bin Liu[2,5,✉]

Cite this article: Fan Y, Bai Y, He X, et al. *J Adv Ceram* 2026, **15**(3): 9221251. https://doi.org/10.26599/JAC.2026.9221251

ABSTRACT: High-entropy rare-earth (RE) disilicates are promising next-generation thermal/environmental barrier coating (T/EBC) materials. However, their resistance to calcium–magnesium–aluminosilicate (CMAS) corrosion and the underlying mechanisms remain insufficiently understood and require further improvement. This study aims to systematically investigate the CMAS corrosion behavior and predictive lifetime assessment of designed stoichiometric $(Er_{1/4}Y_{1/4}Lu_{1/4}Yb_{1/4})_2Si_2O_7$ and non-stoichiometric $(Er_{1/6}Tm_{1/6}Y_{1/15}Gd_{1/15}Lu_{4/15}Yb_{4/15})_2Si_2O_7$. The incorporation of Tm and Gd, characterized by their distinct ionic radii, is designed to enhance their phase stability. Mechanistic analysis reveals that lattice distortion induced by multication doping suppresses CMAS infiltration, while the introduction of larger-radius RE^{3+} ions promotes Ca^{2+} depletion in the CMAS melt, reducing its corrosive activity. A temperature-dependent transition in corrosion mechanisms is also elucidated. Thermodynamic–kinetic competition dominates at 1300 °C, whereas a dissolution–reprecipitation mechanism prevails at 1500 °C due to accelerated ion diffusion. Furthermore, an innovative extended Kalman filter (EKF) model is developed, enabling highly accurate prediction of the long-term corrosion depth and rate at 1300 °C, with an error of less than 3%. The experimental results demonstrate that both materials exhibit exceptional CMAS corrosion resistance, reducing the corrosion depth by approximately 70% compared with single-component $RE_2Si_2O_7$. This work not only clarifies the corrosion mechanisms and compositional design principles of high-entropy rare-earth disilicates but also provides a novel methodology for predictive lifetime assessment, advancing the development of next-generation T/EBC systems.

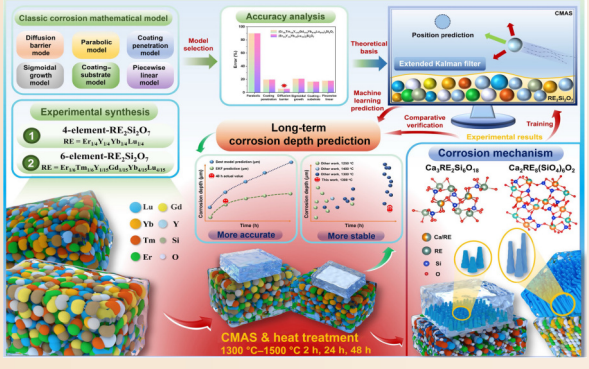

KEYWORDS: high entropy; rare-earth disilicate; environmental barrier coating; extended Kalman filter; calcium–magnesium–aluminosilicate resistance

1 Introduction

The global economic impact of corrosion is substantial, accounting for an estimated 3%–4% of a nation's gross domestic product (GDP); total worldwide costs reached $2.5 trillion in 2013 [1]. Consequently, there are significant economic incentives to mitigate corrosion through the development of resistant materials and the improved understanding of underlying mechanisms [2]. A significant approach to address high-temperature corrosion involves the application of thermal/environmental barrier coatings (T/EBCs) onto ceramic matrix composite (CMC) components in gas-turbine engines, which are critical for both aircraft propulsion and power generation [3–5]. However, their engineering applications and reliability are constrained by severe corrosion in high-temperature environments, particularly from water vapor and molten calcium–magnesium–aluminum–silicate (CMAS) deposits [6–11]. Rare-earth disilicates ($RE_2Si_2O_7$) are promising T/EBC materials owing to their matched coefficient of thermal expansion with CMCs, high damage tolerance, and good resistance to both water vapor and CMAS corrosion [12]. Nevertheless, conventional single-component $RE_2Si_2O_7$ still faces challenges such as phase transitions and thermal stress induced by CMAS corrosion, limiting their further application [13].

High-entropy ceramics exhibit properties superior to those of single-component materials due to high-entropy effects, sluggish diffusion, lattice distortion, and cocktail effects [14–17], offering

[1] National Key Laboratory of Science and Technology on Advanced Composites in Special Environments and Center for Composite Materials and Structure, Harbin Institute of Technology, Harbin 150080, China. [2] School of Materials Science and Engineering, Shanghai University, Shanghai 200444, China. [3] School of Electronics and Information Engineering, Harbin Institute of Technology, Harbin 150080, China. [4] College of Sciences, Nanjing Agricultural University, Nanjing 210095, China. [5] Institute of Coating Technology for Hydrogen Gas Turbines, Liaoning Academy of Materials, Shenyang 110004, China.

✉ Corresponding authors. E-mail: Y. Bai, baiyl@hit.edu.cn; B. Liu, binliu@shu.edu.cn

Received: October 27, 2025; Revised: January 11, 2026; Accepted: January 14, 2026

new strategies for T/EBC design. Specifically, for CMAS corrosion resistance, the pronounced lattice distortion in high-entropy ceramics can hinder ion diffusion and melt infiltration, while the cocktail effect enables synergistic optimization of reactivity and stability through strategic elemental combinations. Previous studies have demonstrated that high-entropy rare-earth disilicates ($(nRE_{xi})_2Si_2O_7$) can reduce the coefficient of thermal expansion and thermal conductivity while enhancing phase stability and corrosion resistance [14,18,19]. The corrosion of $(nRE_{xi})_2Si_2O_7$ by CMAS primarily follows a "dissolution–reprecipitation" process: The material first dissolves into the molten CMAS, and then Ca–RE–Si–O products (e.g., cyclosilicates, apatite) precipitate once $REO_{1.5}$ reaches saturation, inhibiting further corrosion by consuming Ca^{2+} ions or forming a barrier layer [20–22]. For instance, Dong *et al.* [23] showed that a high-entropy disilicate forms a dense cyclosilicate layer at 1400 °C, suppressing CMAS corrosion. However, this pioneering study is limited to a single temperature and composition. To establish a more comprehensive understanding, our study systematically investigates the temperature-dependent corrosion behavior across a wider range (1300–1500 °C), covering both typical and extreme service conditions for T/EBC applications. Furthermore, we have specifically designed our material compositions to address key research gaps. This enables us to systematically probe the effects of compositional complexity on corrosion mechanisms across different temperatures. In this process, the stoichiometry of the material influences RE^{3+} solubility, reactivity, and the phase composition of the product layer. Specifically, non-stoichiometric materials may modulate element diffusion and corrosion kinetics by tailoring defect concentrations. Although these studies confirm that high-entropy design can improve CMAS resistance, critical research gaps remain: (1) The intrinsic relationship between microstructure (e.g., lattice distortion, equivalent ionic radius) and CMAS corrosion resistance is not systematically elucidated; (2) current research on high-entropy rare-earth disilicates is limited to stoichiometric compositions, but the corrosion behavior and regulatory mechanisms of non-stoichiometric high-entropy rare-earth disilicates are still unclear. To address these identified research gaps, we designed two distinct high-entropy disilicate compositions with specific structural characteristics. Stoichiometric $(Er_{1/4}Y_{1/4}Lu_{1/4}Yb_{1/4})_2Si_2O_7$ serves as an ideal system to systematically investigate the relationship between microstructure and CMAS resistance. This composition creates a controlled lattice environment with well-defined distortion characteristics, allowing us to quantitatively correlate the degree of lattice distortion and the equivalent ionic radius with CMAS corrosion resistance through comparative analysis with the non-stoichiometric counterpart. The controlled chemical environment in this four-component system enables unambiguous identification of how lattice distortion influences CMAS melt infiltration and reaction kinetics. Meanwhile, the non-stoichiometric $(Er_{1/6}Tm_{1/6}Y_{1/15}Gd_{1/15}Lu_{4/15}Yb_{4/15})_2Si_2O_7$, incorporating six rare-earth elements with deliberately varied molar ratios, is specifically designed to address the unknown corrosion behavior of non-stoichiometric high-entropy disilicates. The intentional deviation from stoichiometry introduces controlled local chemical heterogeneity, creating a platform to investigate how chemical composition and ratio modulate element diffusion pathways, corrosion product formation, and overall corrosion kinetics. Through comparative analysis of these two strategically designed compositions under identical corrosion conditions, we can provide comprehensive insights into both identified research gaps.

Notably, the long-term service safety of T/EBCs relies on accurate corrosion life assessment, wherein corrosion depth and rate are key metrics. CMAS corrosion is a complex time-varying dynamic process. Traditional predictive models based on parabolic rate laws or other static corrosion models fail to adequately account for influencing factors such as the dynamic evolution of the reaction layer, limiting their predictive accuracy. The extended Kalman filter (EKF) algorithm integrates experimental data with physical models, enabling real-time updates and corrections to parameters and state variables [24,25]. This enhances the prediction reliability for nonlinear, uncertain systems such as high-temperature corrosion processes. However, no studies have yet combined EKF with corrosion models to predict the long-term corrosion behavior of materials. This results in a fundamental bottleneck in predicting the service behavior of T/EBC materials under long-term CMAS corrosion. Due to the inability of traditional static models to capture key time-varying factors such as the dynamic evolution of the reaction layer during the corrosion process, there is a significant deviation in their long-term extrapolation predictions. This bias causes uncertainty in model-based corrosion life assessment, which may lead to increasing costs or threaten application safety.

Based on our previous works, $(Er_{1/4}Y_{1/4}Lu_{1/4}Yb_{1/4})_2Si_2O_7$ and $(Er_{1/6}Tm_{1/6}Y_{1/15}Gd_{1/15}Lu_{4/15}Yb_{4/15})_2Si_2O_7$ were selected for this work. Both have demonstrated excellent thermomechanical properties and phase stability [26]. Additionally, the resistance to CMAS corrosion can be enhanced by increasing the proportion of inert elements (Yb, Lu), maintaining the ratio of neutral elements (Ho, Er, Tm), and reducing the content of other rare-earth elements (La, Ce, Y, Eu). Furthermore, the CMAS corrosion resistance of both materials is systematically investigated at 1300 and 1500 °C, and their corrosion behaviors at these temperatures are compared, as shown in Fig. 1. The regulatory mechanisms of composition and corrosion temperature on the corrosion process are revealed through analysis of corrosion products and microstructural evolution. Meanwhile, an EKF algorithm is innovatively introduced, combined with a classical corrosion kinetics model, to establish a predictive model for long-term corrosion depth and rate at 1300 °C. This study aims to achieve dynamic and high-precision prediction of material corrosion behavior, providing theoretical support and experimental evidence for the design and service life assessment of next-generation high-performance T/EBC high-entropy rare-earth disilicate materials.

2 Method

2.1 Experimental

2.1.1 *Sample preparation*

Commercial oxides, including Lu_2O_3, Er_2O_3, Y_2O_3, Tm_2O_3, and SiO_2 (99.9%, Aladdin), as well as Gd_2O_3 and Yb_2O_3 (99.99%, Aladdin), were used as starting materials to synthesize $(Er_{1/4}Y_{1/4}Lu_{1/4}Yb_{1/4})_2Si_2O_7$ and $(Er_{1/6}Tm_{1/6}Y_{1/15}Gd_{1/15}Lu_{4/15}Yb_{4/15})_2Si_2O_7$. To account for possible SiO_2 loss due to volatilization, the molar ratio of RE_2O_3 to SiO_2 was set at 1 : 1.05. The precursors were planetary ball-milled at 250 r/min for 24 h using agate balls and ethanol as the grinding medium. The resulting slurry was then dried at 60 °C for 12 h. Phase-pure products were obtained after pressureless sintering at 1600 °C for 4 h. To fabricate dense bulk ceramics, the synthesized powders were ball-milled again for 12 h, dried, and subsequently densified by hot-pressing in BN-coated graphite molds at 1700 °C for 2 h under a uniaxial pressure of 30 MPa in vacuum, yielding $(nRE_{xi})_2Si_2O_7$ bulks. Compared with direct hot-pressing of the reactant mixture, the two-step method offers two advantages. First, pressureless sintering ensures

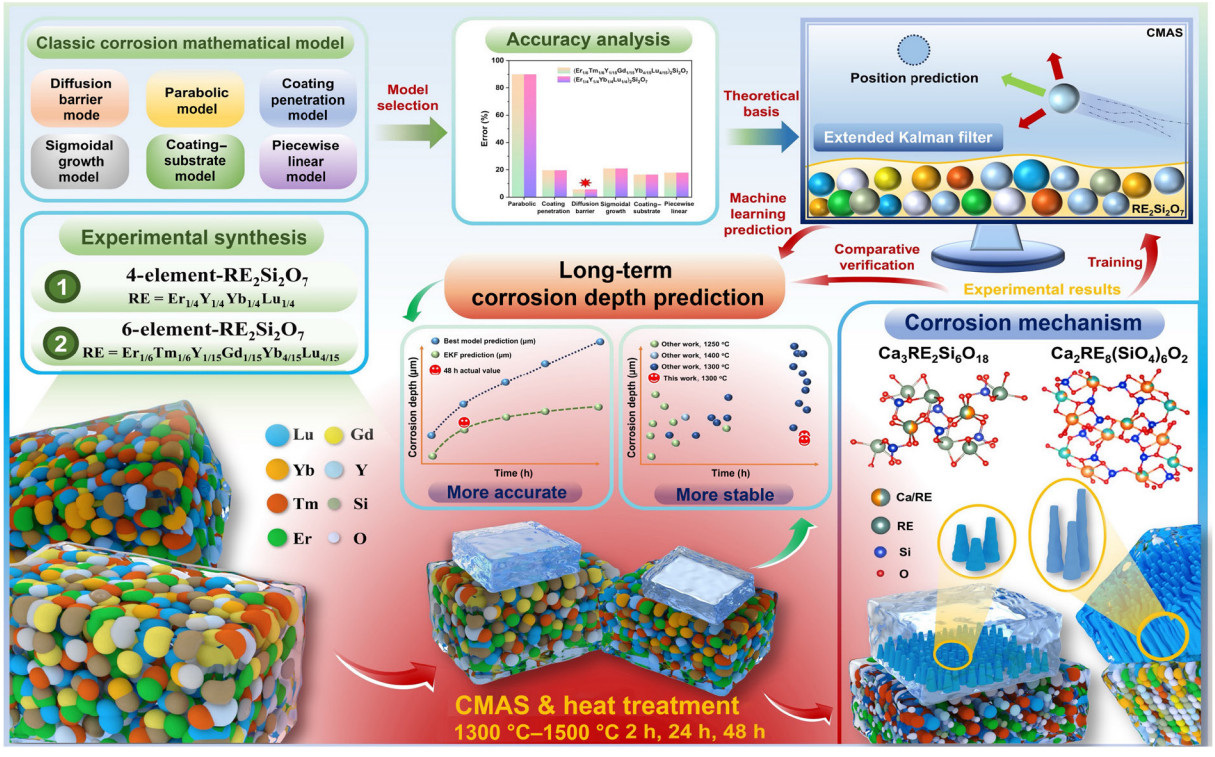

Fig. 1 Workflow diagram for this work.

the synthesis of pure-phase high-entropy silicates and avoids potential carbon contamination or non-equilibrium reactions from the graphite die. Second, the synthesized powder was re-milled to de-agglomerate the clusters, producing finer particles with higher sintering activity that facilitated the fabrication of high-density bulk ceramics.

2.1.2 *Characterization*

An X-ray diffractometer (XRD; PANalytical B.V., Netherlands) using Cu Kα radiation was used to identify the phase composition of both the as-prepared samples and the corrosion products. The measurements were carried out over a 2θ range of 10°–70° with a step size of 0.02° and a scanning rate of 2 (°)/min. Microstructural characterization and elemental analysis were conducted using a scanning electron microscope (SEM; Merlin Compact, Carl Zeiss AG, Germany) equipped with an energy-dispersive X-ray spectroscopy (EDS) detector. Lattice parameters were refined by Rietveld analysis implemented in the GSAS software package, and the bulk density (ρ) was measured via the Archimedes method. The Vickers hardness was measured by a micro indentation tester (HXD-1000TMC/LCD, Shanghai Qinming Optical Instrument Co., Ltd., China) with various applied loads and holding time of 10 s.

2.1.3 *CMAS corrosion*

A CMAS composition of 33CaO–9MgO–13Al_2O_3–45SiO_2, representative of typical deposits encountered in aviation environments, was selected for corrosion tests [25]. The CMAS powder was synthesized by mixing stoichiometric amounts of CaO, MgO, Al_2O_3, and SiO_2, followed by calcination at 1300 °C for 2 h to form a homogeneous glassy phase. As confirmed by XRD patterns (Fig. S1 in the Electronic Supplementary Material (ESM)), the resulting product was predominantly amorphous. In the corrosion experiments, a uniform CMAS coating (30 mg/cm^2) was applied onto the ceramic surface. A slurry was prepared by mixing CMAS powder with anhydrous ethanol, which was then evenly applied to the sample surface. The sample weight was accurately measured before and after coating to control the CMAS loading. After the ethanol completely evaporated in air, the samples were then heat-treated in a muffle furnace at 1300 or 1500 °C for 2–48 h (heating rate: 10 °C/min). After corrosion, cross-sectional specimens were prepared by grinding and polishing for SEM examination. The thickness of the reaction layer was determined by averaging measurements taken at five different locations. To analyze the crystalline reaction products, powder mixtures of $(nRE_{xi})_2Si_2O_7$ and CMAS at a mass ratio of 4 : 1 were heat-treated at 1300 °C for 2 h and 1500 °C for 2 and 48 h, respectively, prior to XRD analysis.

2.2 Computational details

2.2.1 *DFT calculations*

All density functional theory (DFT) calculations in this study were carried out with the Vienna *ab initio* simulation package (VASP) [27,28]. The projector augmented wave (PAW) method was employed to describe electron–ion interactions using a plane-wave energy cutoff of 520 eV to ensure energy convergence within 1 meV/atom. The valence configurations were set as $5p^6 5d^1 6s^2$ for RE elements, $3s^2 3p^2$ for Si, and $2s^2 2p^4$ for O. The Perdew–Burke–Ernzerhof (PBE) functional within the generalized gradient approximation (GGA) was applied to account for exchange-correlation effects. A Γ-centered 2 × 3 × 2 Monkhorst–Pack *k*-point mesh was used for sampling the Brillouin zone. Since the geometric structure and lattice parameters show a weak dependence on the *U* parameter, the effects of *U* were consequently neglected in the calculations [27,28]. All structures were relaxed, including atomic positions, cell volume, and shape, until the energy change between electronic steps was less than 10^{-6} eV and the maximum force on any atom was below 0.01 eV/Å.

To model $(nRE_{xi})_2Si_2O_7$, special quasirandom structures (SQS) were generated using Monte Carlo simulations, in which random

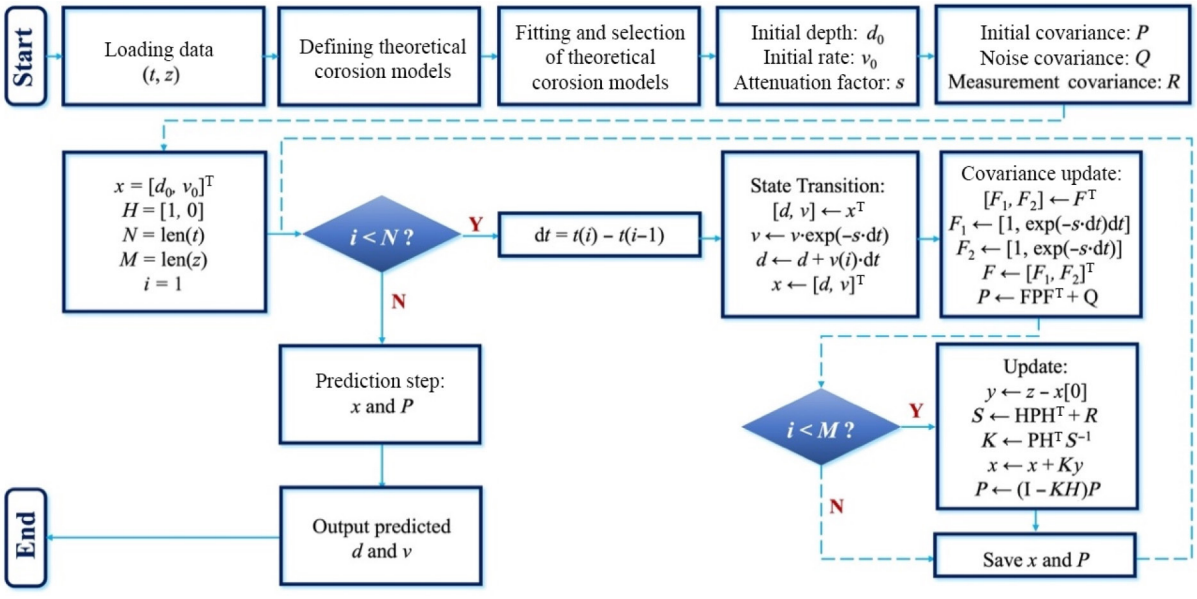

Fig. 2 Schematic diagram of extended Kalman filter framework designed to accelerate prediction of corrosion depth in long-term corrosive environments.

swaps were permitted only among cation sublattices, without involving anion sites [29,30]. For each composition, three independent SQS configurations were constructed and evaluated to ensure convergence in both lattice constants and energies with respect to local chemical environments.

2.2.2 *Extended Kalman filter*

To address the prediction of the corrosion depth and rate in long-term corrosive environments, an extended Kalman filter was employed based on classical mathematical corrosion models to predict the corrosion depth and rate at different temperature points (beyond 24 h), including the diffusion barrier model, parabolic model, coating penetration model, S-shaped growth model, coating-substrate combined model, and piecewise linear model [31,32]. Detailed descriptions of these models are provided in Note 1 in the ESM.

As shown in Fig. 2, experimental corrosion depth data at 1300 °C for 0–24 h were used to fit the mathematical corrosion models. The optimal model was determined by evaluating fitting errors and comparing the predicted corrosion depth at 48 h with experimental values at 1300 °C. Subsequently, the extended Kalman filter was applied to handle the inherent nonlinearity of the corrosion process. The EKF algorithm consists of two iterative steps: prediction and update. In the prediction step, the selected corrosion model performs forward propagation on the state vector (including depth and velocity) and its covariance matrix. Due to the nonlinear nature of corrosion kinetics, the Jacobian matrix of the model function was computed to linearize the system around the current state estimate. Among them, the measurement noise covariance (R) was determined based on the experimental error in the thickness measurement of the reaction layer. Meanwhile, the process noise covariance Q was empirically tuned according to the residuals between the model predictions and the short-term experimental data. In the update step, the predicted state was corrected by integrating measurement data, and the covariance matrix was updated to quantify process and measurement uncertainties. Through this recursive estimation approach, the EKF enables accurate identification of model parameters and reliable long-term prediction of corrosion depth and rate, even under time-varying and nonlinear corrosion conditions.

3 Results and discussion

3.1 Microstructures and crystals of two $(n\mathrm{RE}_{xi})_2\mathrm{Si}_2\mathrm{O}_7$

Figure 3(c) displays the XRD patterns of $(Er_{1/4}Y_{1/4}Lu_{1/4}Yb_{1/4})_2Si_2O_7$ and $(Er_{1/6}Tm_{1/6}Y_{1/15}Gd_{1/15}Lu_{4/15}Yb_{4/15})_2Si_2O_7$, along with the standard pattern of β-$Er_2Si_2O_7$ for comparison. The diffraction results confirm the formation of a single-phase solid solution crystallized in a β-type crystal structure. As the temperature increases, no additional impurity peaks appear. Figures 3(a) and 3(b) show SEM images of the $(Er_{1/4}Y_{1/4}Lu_{1/4}Yb_{1/4})_2Si_2O_7$ and $(Er_{1/6}Tm_{1/6}Y_{1/15}Gd_{1/15}Lu_{4/15}Yb_{4/15})_2Si_2O_7$ samples, both exhibiting a single-phase microstructure composed of finely arranged polyhedral grains. The as-sintered materials reach densities of 5.48 and 5.79 g/cm^3, respectively, corresponding to a high relative density exceeding 97%. Elemental distribution maps obtained by EDS (Figs. 3(a) and 3(b)) demonstrate a uniform distribution of each element, which further confirms the synthesis of a single-phase solid solution.

To further investigate the crystal details of the two materials, DFT calculations were performed to obtain their structural information. As illustrated in Fig. 3(e), the β-$RE_2Si_2O_7$ structure consists of stacked [REO_6] and [SiO_4] polyhedra [33]. The lattice parameters of the synthesized $(n\mathrm{RE}_{xi})_2Si_2O_7$ compounds in Table 1 are consistent with the experimental results obtained from the XRD refinement, as shown in Table S1 in the ESM. In addition, the configuration entropy (ΔS), mean ionic radius ($\bar{r}$), and ionic radius deviation (σ_r) are summarized in Table 1, with details provided in Note 2 in the ESM [34]. The results indicate that ΔS depends solely on the number and proportion of RE species incorporated, while $\bar{r}$ and σ_r are influenced by the specific types of rare-earth ions. Specifically, larger ionic radii tend to increase $\bar{r}$, while greater disparities among the ionic radii lead to higher σ_r values. The incorporation of multiple RE ions disrupts the atomic equilibrium due to variations in their ionic radii, thereby inducing lattice distortion. To quantitatively assess this distortion, the distortion index (Δd) is evaluated using Eq. (1) [35]:

$$\Delta d = \frac{1}{n}\sum_{n}\left(\frac{d(L-O)_n - \overline{d(L-O)}}{\overline{d(L-O)}}\right)^2 \quad (1)$$

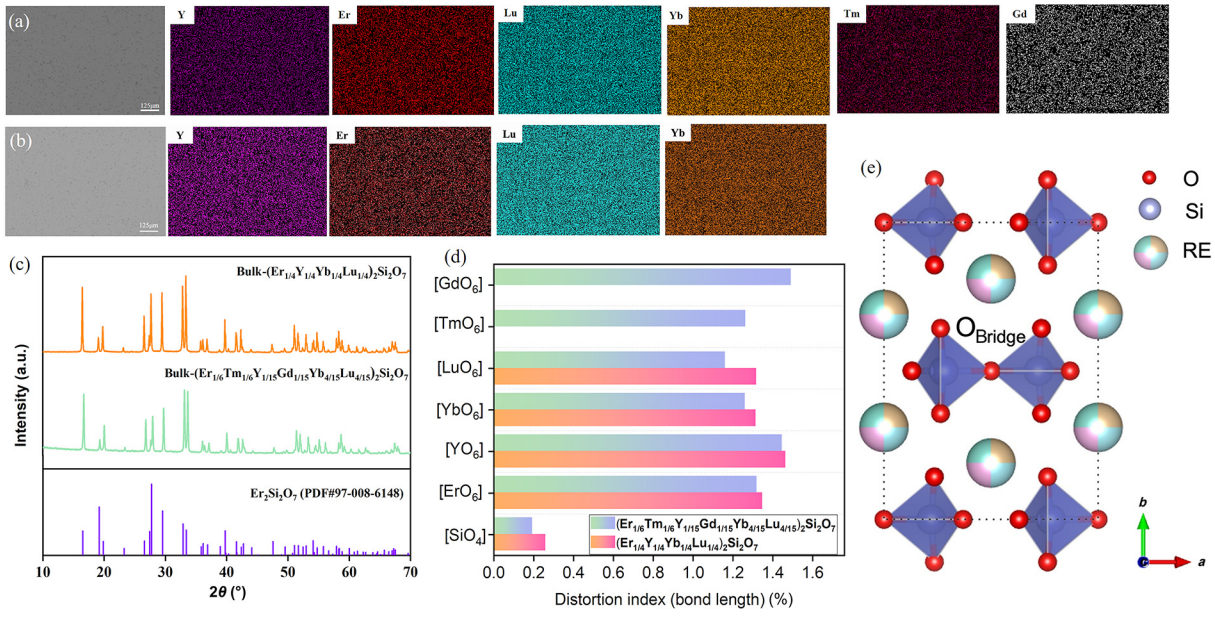

Fig. 3 SEM images and EDS mappings of (a) $(Er_{1/6}Tm_{1/6}Y_{1/15}Gd_{1/15}Lu_{4/15}Yb_{4/15})_2Si_2O_7$ and (b) $(Er_{1/4}Y_{1/4}Lu_{1/4}Yb_{1/4})_2Si_2O_7$. (c) XRD results, (d) crystal distortion, and (e) crystal structure of $(Er_{1/4}Y_{1/4}Lu_{1/4}Yb_{1/4})_2Si_2O_7$ and $(Er_{1/6}Tm_{1/6}Y_{1/15}Gd_{1/15}Lu_{4/15}Yb_{4/15})_2Si_2O_7$.

Table 1 Crystal features of $(Er_{1/4}Y_{1/4}Lu_{1/4}Yb_{1/4})_2Si_2O_7$ and $(Er_{1/6}Tm_{1/6}Y_{1/15}Gd_{1/15}Lu_{4/15}Yb_{4/15})_2Si_2O_7$

Composite	$(Er_{1/4}Y_{1/4}Lu_{1/4}Yb_{1/4})_2Si_2O_7$	$(Er_{1/6}Tm_{1/6}Y_{1/15}Gd_{1/15}Lu_{4/15}Yb_{4/15})_2Si_2O_7$
a (Å)	6.77	6.78
b (Å)	8.84	8.86
c (Å)	4.74	4.75
$\bar{r}$ (Å)	0.880	0.879
σ_r	0.02	0.02
ΔS (J·mol^{-1}·K^{-1})	1.39R	1.66R

where $d(L-O)$ represents the bond distance between cation L (L = RE or Si) and the nth oxygen atom and $\overline{d(L-O)}$ denotes the corresponding mean bond length. Figure 3(d) shows the calculated distortion indexes for the [REO_6] and [SiO_4] polyhedra in $(Er_{1/4}Y_{1/4}Lu_{1/4}Yb_{1/4})_2Si_2O_7$ and $(Er_{1/6}Tm_{1/6}Y_{1/15}Gd_{1/15}Lu_{4/15}Yb_{4/15})_2Si_2O_7$. In the crystal structure of $(nRE_{xi})_2Si_2O_7$, the coexistence of multiple RE cations with differing ionic radii at equivalent atomic sites not only distorts the [REO_6] polyhedra but also exerts compressive or tensile effects on the [SiO_4] tetrahedra, further contributing to structural distortion [28]. Specifically, an increase in σ_r and $\bar{r}$ corresponds to greater lattice distortion in both the [REO_6] and [SiO_4] polyhedra [36].

3.2 CMAS corrosion resistance of two $(nRE_{xi})_2Si_2O_7$ at 1300 °C

3.2.1 Corrosion morphology and phase of two $(nRE_{xi})_2Si_2O_7$ at 1300 °C

Figure 4 presents cross-sectional SEM images of $(Er_{1/4}Y_{1/4}Lu_{1/4}Yb_{1/4})_2Si_2O_7$ and $(Er_{1/6}Tm_{1/6}Y_{1/15}Gd_{1/15}Lu_{4/15}Yb_{4/15})_2Si_2O_7$ after CMAS corrosion at 1300 °C for 2 h. Both the $(Er_{1/4}Y_{1/4}Lu_{1/4}Yb_{1/4})_2Si_2O_7$ and $(Er_{1/6}Tm_{1/6}Y_{1/15}Gd_{1/15}Lu_{4/15}Yb_{4/15})_2Si_2O_7$ samples exhibit a three-layer structure consisting of a residual CMAS layer, a reaction product layer, and an intact ceramic substrate. Notably, the reaction layer of $(Er_{1/4}Y_{1/4}Lu_{1/4}Yb_{1/4})_2Si_2O_7$ contains both rod-like and dendritic morphologies, whereas only rod-shaped products are observed in the $(Er_{1/6}Tm_{1/6}Y_{1/15}Gd_{1/15}Lu_{4/15}Yb_{4/15})_2Si_2O_7$ sample. EDS analysis at points 1–3 (Table 2) confirms the presence of RE, Ca, and Si elements at the corrosion front. The dendritic regions exhibit a Ca/Si ratio of approximately 1.5, which is higher than that of the rod-like areas (approximately 0.25).

To investigate the corrosion evolution, the corrosion time is extended. As shown in Fig. 5, the corrosion depth increases progressively with time, although the corrosion rate decreases. After 48 h, residual CMAS is observed on both materials. The thinner reaction layer in $(Er_{1/4}Y_{1/4}Lu_{1/4}Yb_{1/4})_2Si_2O_7$ than that in $(Er_{1/6}Tm_{1/6}Y_{1/15}Gd_{1/15}Lu_{4/15}Yb_{4/15})_2Si_2O_7$ suggests its superior corrosion resistance. Morphologically, $(Er_{1/6}Tm_{1/6}Y_{1/15}Gd_{1/15}Lu_{4/15}Yb_{4/15})_2Si_2O_7$ maintains rod-like precipitates over time, while the dendritic structures in $(Er_{1/4}Y_{1/4}Lu_{1/4}Yb_{1/4})_2Si_2O_7$ diminish. Additionally, the apparent densification of the unreacted bulk substrate observed in Fig. 5 after prolonged corrosion at 1300 °C can be attributed to variations inherent in the ceramic samples used for CMAS corrosion testing. Due to microstructural inhomogeneity during the sintering process, such as uneven grain distribution and slight differences in matrix density, indeed exist across different regions. This intrinsic microstructural variation may lead to localized differences in the infiltration rate of the CMAS melt during the corrosion stage, resulting in the observed appearance of a denser bulk substrate after extended corrosion. To identify the Ca–RE–Si reaction products, powder mixtures of $(nRE_{xi})_2Si_2O_7$ and CMAS were calcined at 1300 °C for 2 h. The XRD results shown in Fig. 6(a) reveal the formation of $Ca_3RE_2Si_6O_{18}$ and $Ca_3RE_8(SiO_4)O_2$ phases alongside $(nRE_{xi})_2Si_2O_7$. In summary, the EDS and XRD results suggest that the reaction

Table 2 Element content for each point in Fig. 4 (Unit: at%)

	Ca	Si	Er	Y	Yb	Lu	Gd	Tm	RE
1	10.05	20.02	1.64	1.57	1.53	1.56	—	—	6.30
2	4.56	7.69	4.20	4.27	4.07	3.80	—	—	16.34
3	5.07	9.21	2.96	1.90	4.51	4.48	2.00	2.93	18.78

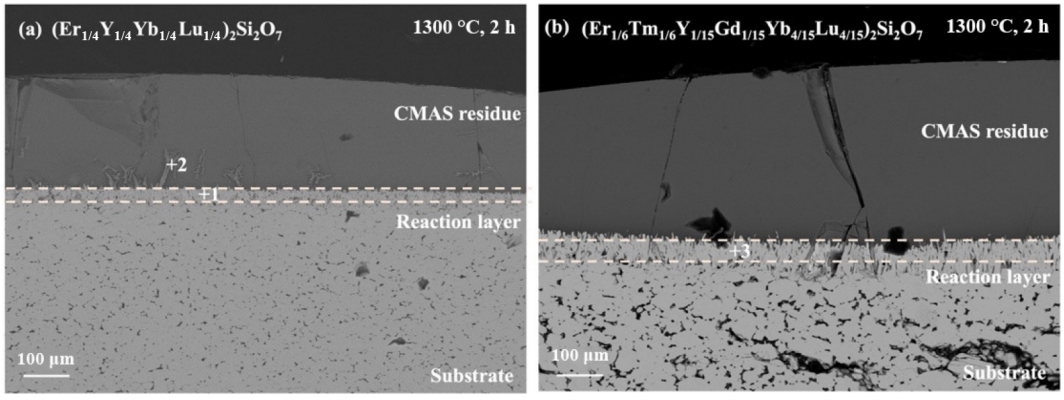

Fig. 4 Cross-section images of (a) $(Er_{1/4}Y_{1/4}Lu_{1/4}Yb_{1/4})_2Si_2O_7$ and (b) $(Er_{1/6}Tm_{1/6}Y_{1/15}Gd_{1/15}Lu_{4/15}Yb_{4/15})_2Si_2O_7$ after CMAS corrosion at 1300 °C for 2 h.

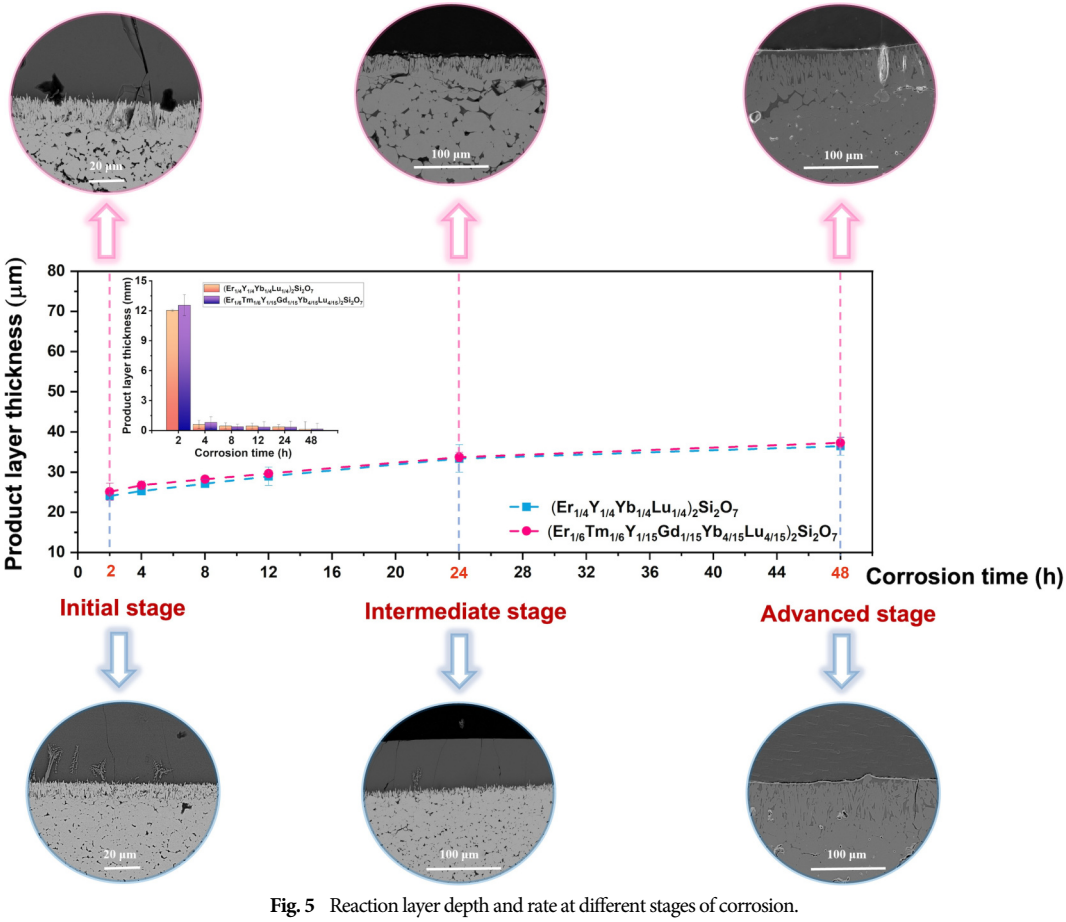

Fig. 5 Reaction layer depth and rate at different stages of corrosion.

layer is likely composed of accumulated cyclosilicate and apatite phases.

3.2.2 *Corrosion mechanism of two $(nRE_{xi})_2Si_2O_7$ at 1300 °C*

During CMAS corrosion, the RE disilicate first dissolves into the molten CMAS, during which RE ions diffuse outward from the dissolution front. Once the Ca/RE ratio reaches a critical threshold, Ca–RE–Si compounds begin to precipitate from the melt [37]. Simultaneously, a reaction product layer forms via a reaction–precipitation mechanism at the corrosion interface, wherein $(nRE_{xi})_2Si_2O_7$ reacts with CaO and SiO_2 in the CMAS to form cyclosilicate and apatite phases. This mechanism is further corroborated by previous studies, as described by Reactions (2-a) and (2-b):

$$RE_2Si_2O_7 + 3CaO\,(CMAS) + 4SiO_2\,(CMAS) \rightarrow Ca_3RE_2Si_6O_{18} \quad (2\text{-a})$$

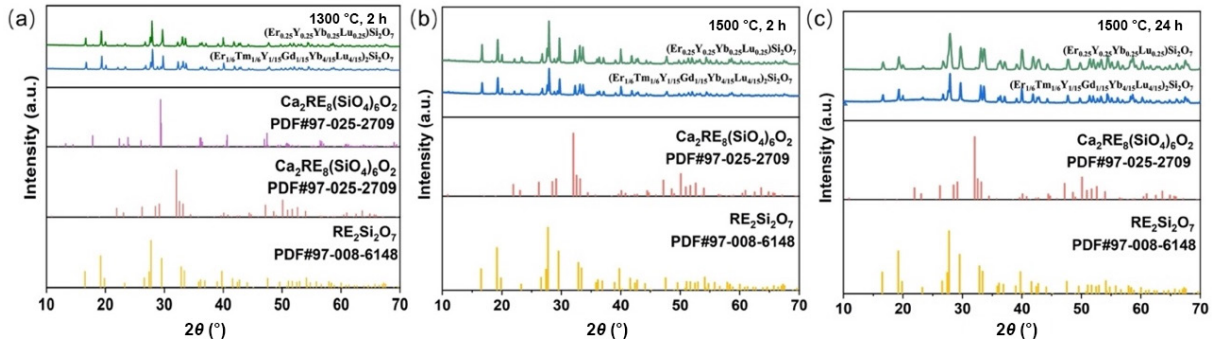

Fig. 6 XRD patterns of $(nRE_{xi})_2Si_2O_7$ and CMAS powder mixtures after calcining at (a) 1300 °C for 2 h, (b) 1500 °C for 2 h, and (c) 1500 °C for 24 h.

$$4RE_2Si_2O_7 + 2CaO\,(CMAS) \rightarrow Ca_2RE_8(SiO_4)_6O_2 + 2SiO_2 \quad (2\text{-}b)$$

For the corrosion products of two $(nRE_{xi})_2Si_2O_7$, in addition to their common corrosion product $Ca_2RE_8(SiO_4)O_2$, the emergence of the $Ca_3RE_2Si_6O_{18}$ phase can be attributed to the relatively high viscosity of the CMAS melt at 1300 °C, which reduces the solubility of the silicate-based matrix. The crystals of $Ca_3RE_2Si_6O_{18}$ and $Ca_2RE_8(SiO_4)O_2$ have Ca/RE ratios of approximately 1.5 and 0.25, respectively. The formation of $Ca_3RE_2Si_6O_{18}$ requires fewer RE^{3+}, explaining its preferential formation in the $(Er_{1/4}Y_{1/4}Lu_{1/4}Yb_{1/4})_2Si_2O_7$ sample during the early corrosion stage. As corrosion progresses, the viscosity of the CMAS melt decreases, leading to an increased dissolution rate of the substrate. The consequent rise in RE^{3+} ion concentration and its graded distribution facilitate the reprecipitation of dissolved matrix components and the formation of apatite. On the other hand, the crystal structural features of $Ca_3RE_2Si_6O_{18}$ and $Ca_2RE_8(SiO_4)O_2$ also contribute. In $Ca_3RE_2Si_6O_{18}$, three crystallographic sites can be occupied by either Ca or RE ions, whereas in $Ca_2RE_8(SiO_4)O_2$, only one site is available for mixed occupation. This results in greater lattice distortion in cyclosilicate, weakening its structural stability. It has been reported that cyclosilicates possess lower stability in CMAS melts than apatite [16]. Therefore, as the reaction proceeds, the system tends to form the more stable $Ca_2RE_8(SiO_4)O_2$ phase rather than $Ca_3RE_2Si_6O_{18}$, leading to a gradual reduction of the latter in $(Er_{1/4}Y_{1/4}Lu_{1/4}Yb_{1/4})_2Si_2O_7$ after a long corrosion time.

To elucidate the corrosion mechanisms and early-stage product differences, we introduced the distortion index and optical basicity (OB), which correlate with the differing corrosion kinetics of the two materials. First, regarding the role of optical basicity, the average ionic radius ($\bar{r}$) influences the material's chemical characteristics. A smaller $\bar{r}$ corresponds to a higher cationic field strength, which renders the oxide more acidic (i.e., lower OB). Lewis acid–base theory holds that reactivity increases with the OB difference between a crystalline oxide and an oxide glass. The difference in OB is used to evaluate the reactivity of RE silicates in CMAS melts by Duffy *et al.* [38], Wolf *et al.* [39] and Tian *et al.* [40]. Consequently, the RE silicates with smaller $\bar{r}$ possess a lower OB and thus exhibit a larger OB difference when contacting the highly basic CMAS melt. For $(Er_{1/6}Tm_{1/6}Y_{1/15}Gd_{1/15}Lu_{4/15}Yb_{4/15})_2Si_2O_7$ with a smaller $\bar{r}$, although the larger OB difference relative to CMAS enhances the thermodynamic driving force for the reaction, the high cationic field strength of this material due to its smaller $\bar{r}$ stabilizes its silicate lattice, thereby increasing the kinetic barrier for dissolution. Ultimately, the enhanced kinetic stability dominates, resulting in a lower net reactivity of the material and promoting the reprecipitation of $(nRE_{xi})_2Si_2O_7$ from the residual CMAS glass. Second, the specific ion effect of Gd^{3+} plays a crucial complementary role. The presence of Gd^{3+}, whose ionic radius is close to that of Ca^{2+}, further facilitates the formation of the apatite phase. The minor mismatch of the ionic radius minimizes the localized lattice strain energy when Gd^{3+} substitutes for Ca^{2+}, making it kinetically more favorable for the nucleation and growth of the apatite phase [16]. Furthermore, during rapid precipitation from CMAS melts, the nucleation energy barrier for apatite crystals is critical. A crystal nucleus that can incorporate RE^{3+} ions into the 4f sites with minimal strain possesses a lower activation energy for formation [16]. The presence of Gd^{3+}, which can occupy both RE sites and Ca sites, promotes the stability of the initial apatite nuclei [16]. This plays a catalytic role in accelerating the crystallization of the apatite phase from the melt.

Regarding the difference in corrosion depth between the two $(nRE_{xi})_2Si_2O_7$, the high-entropy effect in thermodynamics enhances the stability of rare-earth disilicates and reduces their dissolution rate in CMAS melts. Furthermore, the lattice distortion in the microstructure, quantitatively characterized by the distortion index, induces sluggish diffusion, which mitigates the attack of Ca^{2+} ions on $(nRE_{xi})_2Si_2O_7$ [6]. It inhibits the reaction among $(nRE_{xi})_2Si_2O_7$, CaO, and SiO_2 at the corrosion front. Therefore, the reactivity of $(nRE_{xi})_2Si_2O_7$ with CMAS is governed by the lattice distortion resulting from multiprincipal RE doping. Large lattice distortion suppresses the formation of cyclosilicate reaction products at the corrosion front, thereby reducing the thickness of the reaction product layer. As shown in Fig. 5, the variation in reaction layer thickness between the two samples exhibits an inverse correlation with the degree of lattice distortion. Namely, $(Er_{1/4}Y_{1/4}Lu_{1/4}Yb_{1/4})_2Si_2O_7$ exhibits greater lattice distortion than $(Er_{1/6}Tm_{1/6}Y_{1/15}Gd_{1/15}Lu_{4/15}Yb_{4/15})_2Si_2O_7$ (Fig. 3(d)), resulting in a thinner reaction layer and better corrosion resistance than those of $(Er_{1/6}Tm_{1/6}Y_{1/15}Gd_{1/15}Lu_{4/15}Yb_{4/15})_2Si_2O_7$. In summary, the corrosion mechanisms can be understood through the interplay of these identified factors. The cocktail effect synergistically combines reduced reactivity from lattice distortion, sluggish diffusion, and Gd^{3+} catalysis of apatite. This integrated perspective clarifies how compositional design governs corrosion behavior.

A dense Ca–RE–Si reaction product layer can serve as an effective physical barrier, inhibiting the further penetration and corrosion of the substrate by molten CMAS and thereby enhancing the material's resistance to high-temperature corrosion. This type of reaction layer improves the overall corrosion resistance by hindering mass exchange and chemical reactions between the CMAS melt and the substrate. To understand CMAS corrosion mechanisms and design high-performance corrosion-resistant materials, we performed elemental mapping on two material cross sections (Figs. 7 and 8). The results indicate that in both the $(Er_{1/4}Y_{1/4}Lu_{1/4}Yb_{1/4})_2Si_2O_7$ and $(Er_{1/6}Tm_{1/6}Y_{1/15}Gd_{1/15}Lu_{4/15}Yb_{4/15})_2Si_2O_7$ samples, the rare-earth elements (including Tm, Y,

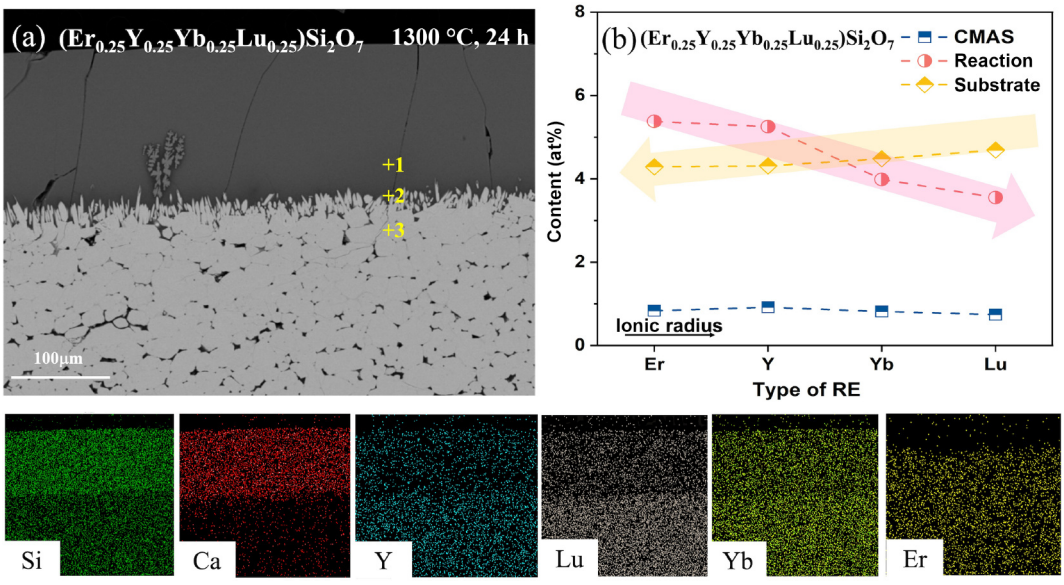

Fig. 7 (a) EDS mappings and (b) content of RE elements of different regions in (a) $(Er_{1/4}Y_{1/4}Lu_{1/4}Yb_{1/4})_2Si_2O_7$ at 1300 °C for 24 h.

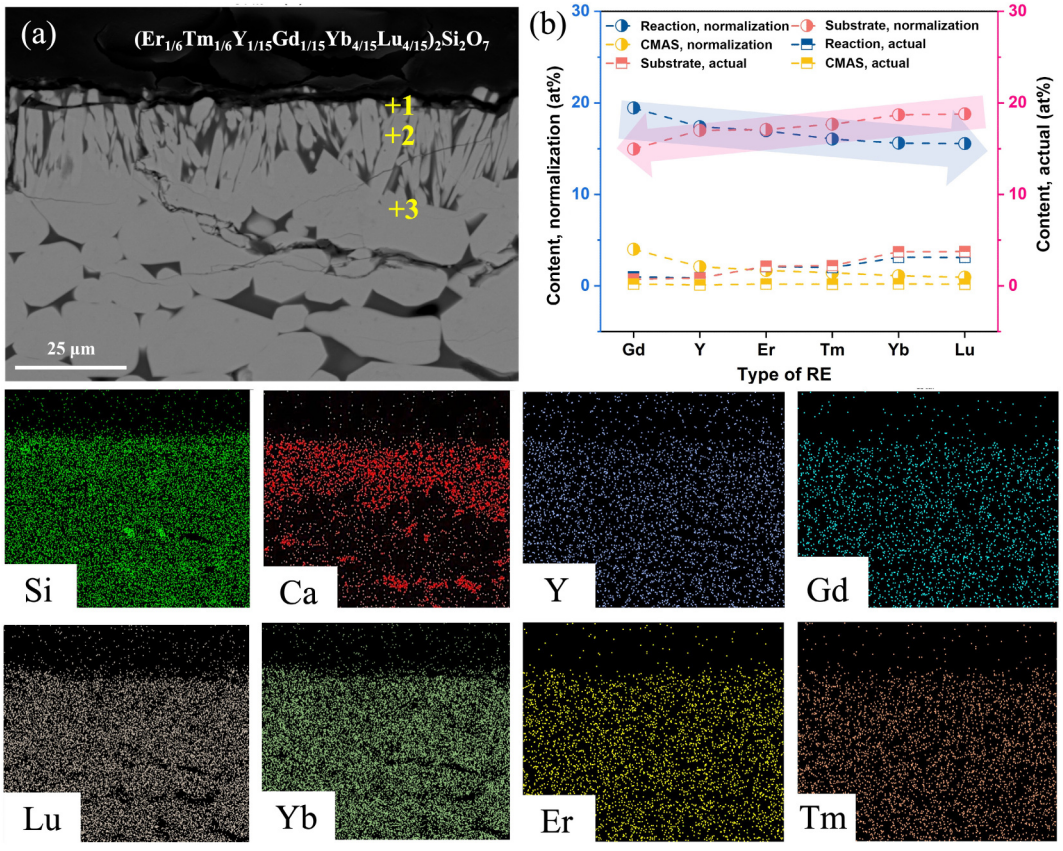

Fig. 8 (a) EDS mappings and (b) content of RE elements of different regions in (a) $(Er_{1/6}Tm_{1/6}Y_{1/15}Gd_{1/15}Lu_{4/15}Yb_{4/15})_2Si_2O_7$ after CMAS corrosion at 1300 °C for 24 h.

Yb, Er, Lu, and Gd) are predominantly distributed within the high-entropy silicate phase and the apatite phase. In contrast, Ca and Si are mainly retained in the residual CMAS melt region and show a tendency to diffuse further into the substrate (Figs. 7(a) and 8(a)). The distributions of Mg and Al elements are provided in Fig. S2 in the ESM. Point analysis revealed that rare-earth elements with smaller atomic radii (such as Lu and Yb) are enriched in the region of the corrosion reaction layer closer to the substrate, whereas those with larger radii (such as Er and Y) are more distributed in the upper part of the reaction layer. To further clarify the distribution differences of elements across various regions, point scanning was conducted for compositional analysis of the bulk layers. Figure 7(b) shows a gradient in rare-earth elements for $(Er_{1/4}Y_{1/4}Lu_{1/4}Yb_{1/4})_2Si_2O_7$: Content decreases with atomic radius in the upper layers but increases in the substrate. For $(Er_{1/6}Tm_{1/6}Y_{1/15}Gd_{1/15}Lu_{4/15}Yb_{4/15})_2Si_2O_7$, the actual elemental ratios remain close to stoichiometric in each layer. However, after normalizing the content, Fig. 8(b) reveals a similar distribution trend.

The above phenomenon is due to the higher solubility and

faster migration of smaller rare-earth ions in the CMAS melt, resulting in a gradient where smaller ions are found farther from the corrosion front. Specifically, in the $(Er_{1/6}Tm_{1/6}Y_{1/15}Gd_{1/15}Lu_{4/15}Yb_{4/15})_2Si_2O_7$ system, the highly active Gd^{3+} ion, with an ionic radius close to that of Ca^{2+}, readily participates in the formation of the apatite phase at the corrosion front. In contrast, the less reactive Lu^{3+} and Yb^{3+} ions, which are relatively insensitive to CMAS corrosion, tend to remain within the substrate lattice, ultimately resulting in a distinct three-layer corrosion structure [35]. As the corrosion time increases, more silicate grains reprecipitate in the residual CMAS glass, leading to gradual thickening of the apatite layer. Therefore, adding larger RE^{3+} ions (e.g., Y and Gd) into high-entropy disilicates enhances corrosion resistance. This helps consume Ca^{2+} via ion exchange and reduces the chemical activity of the CMAS melt. This also explains the inferior corrosion resistance of $(Er_{1/6}Tm_{1/6}Y_{1/15}Gd_{1/15}Lu_{4/15}Yb_{4/15})_2Si_2O_7$ compared with $(Er_{1/4}Y_{1/4}Lu_{1/4}Yb_{1/4})_2Si_2O_7$ at the early corrosion stage. Namely, the low content of Gd and Y in $(Er_{1/6}Tm_{1/6}Y_{1/15}Gd_{1/15}Lu_{4/15}Yb_{4/15})_2Si_2O_7$ is insufficient to enhance corrosion resistance. Based on these results, we propose a design strategy to achieve CMAS resistance by selecting rare-earth elements with a large average ionic radius and maximizing ionic radius differences to enhance lattice distortion and by adding larger RE^{3+} ions to deplete Ca^{2+} in CMAS and reduce its activity.

3.3 CMAS corrosion resistance of two $(nRE_{xi})_2Si_2O_7$ at 1500 °C

3.3.1 Corrosion morphology and phase of two $(nRE_{xi})_2Si_2O_7$ at 1500 °C

To further investigate the CMAS corrosion behavior of the materials at elevated temperatures, $(Er_{1/4}Y_{1/4}Lu_{1/4}Yb_{1/4})_2Si_2O_7$ and $(Er_{1/6}Tm_{1/6}Y_{1/15}Gd_{1/15}Lu_{4/15}Yb_{4/15})_2Si_2O_7$ are subjected to corrosion experiments at 1500 °C for 2 and 24 h. Figures 9(a) and 9(c) show the cross-sectional morphologies and elemental distributions of the $(Er_{1/4}Y_{1/4}Lu_{1/4}Yb_{1/4})_2Si_2O_7$ and $(Er_{1/6}Tm_{1/6}Y_{1/15}Gd_{1/15}Lu_{4/15}Yb_{4/15})_2Si_2O_7$ samples after corrosion at 1500 °C for 2 h. The reaction layer of $(Er_{1/4}Y_{1/4}Lu_{1/4}Yb_{1/4})_2Si_2O_7$ is thinner than that of $(Er_{1/6}Tm_{1/6}Y_{1/15}Gd_{1/15}Lu_{4/15}Yb_{4/15})_2Si_2O_7$, indicating that $(Er_{1/4}Y_{1/4}Lu_{1/4}Yb_{1/4})_2Si_2O_7$ maintains better resistance to CMAS corrosion even at 1500 °C. Moreover, numerous needle-like and blocky corrosion products are visible within the residual CMAS glass adhered to the sample surfaces, suggesting that both materials exhibit good short-term resistance to CMAS attack at high temperature. To identify the composition of the rod-like and blocky corrosion products in the residual CMAS glass, EDS analysis is performed on different phases of the $(Er_{1/4}Y_{1/4}Lu_{1/4}Yb_{1/4})_2Si_2O_7$ and $(Er_{1/6}Tm_{1/6}Y_{1/15}Gd_{1/15}Lu_{4/15}Yb_{4/15})_2Si_2O_7$ samples, and the results are summarized in Fig. 9(e). EDS analysis of the rod-like reaction products (spots 1 and 5 in Fig. 9) revealed the presence of RE, Si, and Ca elements, with an RE/Ca atomic ratio close to 4 : 1, confirming this phase as apatite. Notably, the blocky crystalline phases (spots 2 and 4) within the CMAS glass contain significant amounts of RE and Si, with almost no Ca and an RE/Si atomic ratio of approximately 1 : 1, suggesting that these are reprecipitated high-entropy rare-earth disilicate phases rather than Ca–RE–Si reaction products. Additionally, elemental mappings of the cross sections of the two $(nRE_{xi})_2Si_2O_7$ materials after 2 h of corrosion at 1500 °C are presented in Figs. 9(a) and 9(c). Similar to the elemental distribution after corrosion at 1300 °C (Figs. 7 and 8), RE elements (Y, Yb, Er, Lu, and Gd) are primarily present in the rare-earth disilicate and apatite phases, while Ca is mainly distributed within the residual CMAS melt and the apatite phase.

To further study the reaction products, $(Er_{1/4}Y_{1/4}Lu_{1/4}Yb_{1/4})_2Si_2O_7$ and $(Er_{1/6}Tm_{1/6}Y_{1/15}Gd_{1/15}Lu_{4/15}Yb_{4/15})_2Si_2O_7$ powders are mixed separately with CMAS powder and calcined at 1500 °C for 2 h. The phase compositions of the reaction products are shown in Fig. 6(b). In contrast to the results at 1300 °C, both the $(Er_{1/4}Y_{1/4}Lu_{1/4}Yb_{1/4})_2Si_2O_7$ and $(Er_{1/6}Tm_{1/6}Y_{1/15}Gd_{1/15}Lu_{4/15}Yb_{4/15})_2Si_2O_7$ samples produced apatite and reprecipitated rare-earth disilicate phases at 1500 °C. Sun *et al.* [6] also observed the coexistence of reprecipitated high-entropy rare-earth disilicates and apatite $(Ca_2RE_8(SiO_4)_6O_2)$ when studying the CMAS corrosion resistance of $(Er_{1/4}Y_{1/4}Lu_{1/4}Yb_{1/4})_2Si_2O_7$ at 1500 °C. Similarly, Schulz *et al.* [41] reported the reappearance of RE–Si–O phases in rare-earth zirconate systems under CMAS attack and proposed that $RE_2Si_2O_7$ can reprecipitate rather than transform into apatite. It is worth noting that unlike at 1300 °C, no $Ca_3RE_2Si_6O_{18}$ phases are detected in the corrosion products of $(Er_{1/4}Y_{1/4}Lu_{1/4}Yb_{1/4})_2Si_2O_7$ at 1500 °C. This absence is attributed to the greater lattice distortion in $Ca_3RE_2Si_6O_{18}$, which weakens the crystal structure stability. Thus, they tend to transform into more stable apatite phases at higher temperatures.

As the corrosion time extended to 24 h, the amount of residual CMAS decreased (Figs. 9(b) and 9(d)). The layered structure became less distinct, consisting of residual CMAS glass, corrosion products, and the substrate. The $(Er_{1/4}Y_{1/4}Lu_{1/4}Yb_{1/4})_2Si_2O_7$ sample exhibited a thinner reaction layer than the $(Er_{1/6}Tm_{1/6}Y_{1/15}Gd_{1/15}Lu_{4/15}Yb_{4/15})_2Si_2O_7$ sample, indicating relatively better resistance to CMAS corrosion. EDS analysis and elemental mapping (Figs. 9(b) and 9(d)) revealed that the sample is composed mainly of gray $(nRE_{xi})_2Si_2O_7$ grains (spots 3 and 6) and dark gray CMAS glass, suggesting that the CMAS melt penetrated along grain boundaries but did not significantly react with the $(nRE_{xi})_2Si_2O_7$ grains. Combining the distribution of elements, EDS results, and previous studies [16], it can be found that the darker grains of Figs. 9(b) and 9(d) are pores and/or CMAS that penetrate the grain gap, as shown in Fig. S3 in the ESM. Meanwhile, as shown in Fig. S4 in the ESM, the phenomenon of Mg and Al mainly distributed in the CMAS melt has also been reported in previous works [32]. To further examine the reaction products, $(Er_{1/6}Tm_{1/6}Y_{1/15}Gd_{1/15}Lu_{4/15}Yb_{4/15})_2Si_2O_7$ and $(Er_{1/4}Y_{1/4}Lu_{1/4}Yb_{1/4})_2Si_2O_7$ powders were mixed with CMAS powder and calcined at 1500 °C for 24 h. The phase compositions of the reaction products are shown in Fig. 6(c). Notably, only $(nRE_{xi})_2Si_2O_7$ and minor apatite phases are shown in the $(Er_{1/4}Y_{1/4}Lu_{1/4}Yb_{1/4})_2Si_2O_7$ and $(Er_{1/6}Tm_{1/6}Y_{1/15}Gd_{1/15}Lu_{4/15}Yb_{4/15})_2Si_2O_7$ samples. Based on SEM and EDS analysis, the main corrosion products of both materials after the CMAS reaction are reprecipitated $(nRE_{xi})_2Si_2O_7$ and some apatite. The corrosion products at 1500 °C show much more silicate reprecipitation than those at 1300 °C. This is because higher temperatures facilitate the depletion of Ca^{2+} and the enrichment of RE^{3+}.

3.3.2 Corrosion mechanism of two $(nRE_{xi})_2Si_2O_7$ at 1500 °C

The experimental results demonstrate that $(Er_{1/4}Y_{1/4}Lu_{1/4}Yb_{1/4})_2Si_2O_7$ and $(Er_{1/6}Tm_{1/6}Y_{1/15}Gd_{1/15}Lu_{4/15}Yb_{4/15})_2Si_2O_7$ exhibit different corrosion behaviors and phase evolution pathways under CMAS attack at 1500 °C. To further understand the influence of temperature on the corrosion mechanisms, we compare the corrosion processes of the materials at different temperatures, as illustrated in Fig. 10. Under CMAS corrosion at 1300 °C, the corrosion behavior of both materials is primarily governed by a thermodynamic and kinetic competition equilibrium. At this temperature, the relatively low environmental temperature restricts ionic migration, resulting in high viscosity of the CMAS

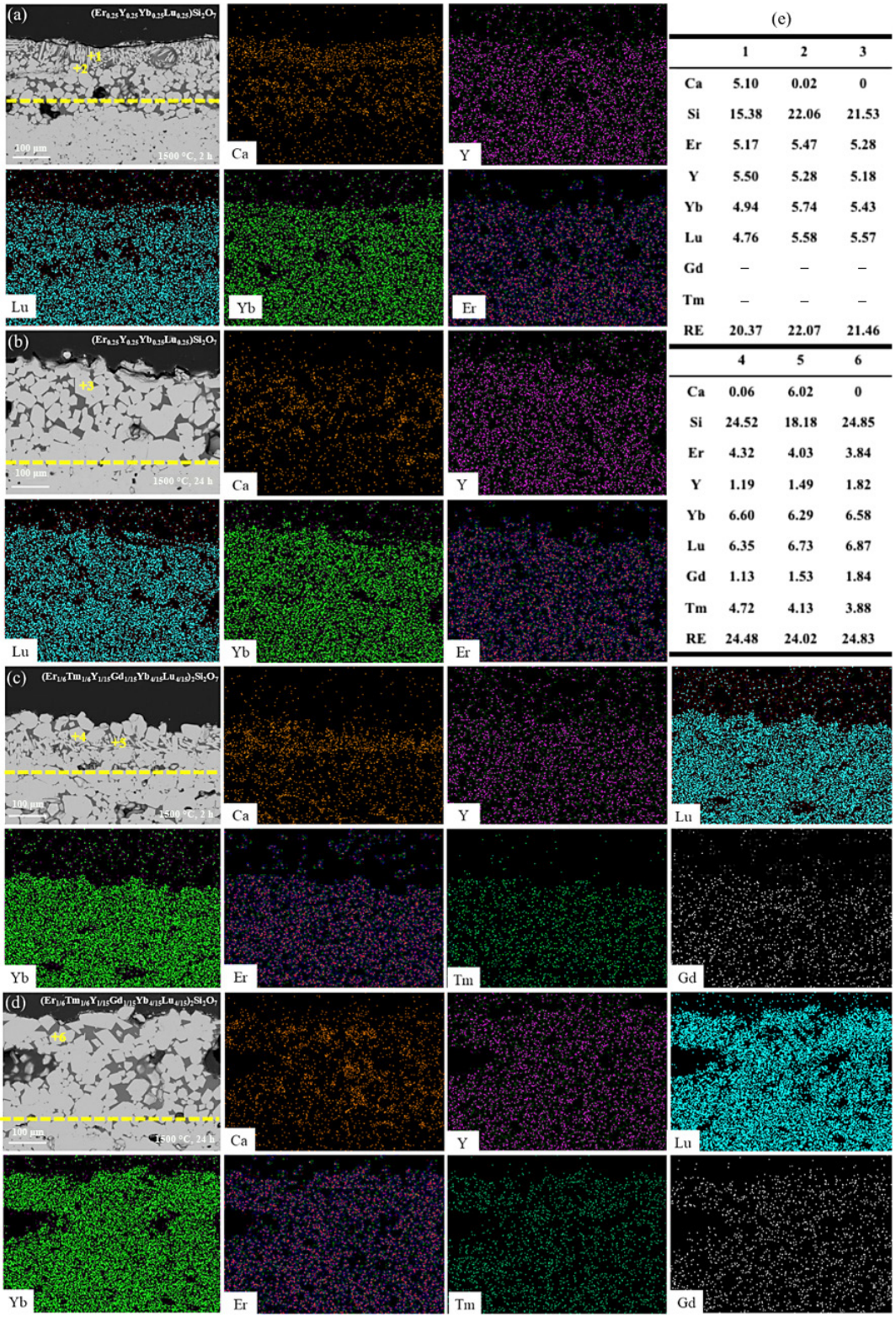

(e)

	1	2	3
Ca	5.10	0.02	0
Si	15.38	22.06	21.53
Er	5.17	5.47	5.28
Y	5.50	5.28	5.18
Yb	4.94	5.74	5.43
Lu	4.76	5.58	5.57
Gd	–	–	–
Tm	–	–	–
RE	20.37	22.07	21.46

	4	5	6
Ca	0.06	6.02	0
Si	24.52	18.18	24.85
Er	4.32	4.03	3.84
Y	1.19	1.49	1.82
Yb	6.60	6.29	6.58
Lu	6.35	6.73	6.87
Gd	1.13	1.53	1.84
Tm	4.72	4.13	3.88
RE	24.48	24.02	24.83

Fig. 9 Cross-sectional images and EDS results of $(Er_{1/4}Y_{1/4}Lu_{1/4}Yb_{1/4})_2Si_2O_7$ and $(Er_{1/6}Tm_{1/6}Y_{1/15}Gd_{1/15}Lu_{4/15}Yb_{4/15})_2Si_2O_7$ after CMAS corrosion at 1500 °C for (a, c) 2 h and (b, d) 24 h.

melt and reduced transport rates of Ca^{2+}. This leads to a slow yet continuous supply of Ca^{2+} at the corrosion interface [35,36]. Such conditions favor the formation and stabilization of the apatite phase. As a thermodynamically stable phase, apatite forms and accumulates at the corrosion front, developing a reaction layer that offers some protective effect, thereby retarding further CMAS penetration and corrosion progression. Hence, at 1300 °C, the apatite phase remains thermodynamically stable, while kinetic diffusion limitations provide the necessary conditions for its formation and persistence.

When the temperature increases to 1500 °C, the corrosion mechanism shifts toward a thermodynamically controlled dissolution–reprecipitation process. The high-temperature environment reduces the viscosity of the CMAS melt and

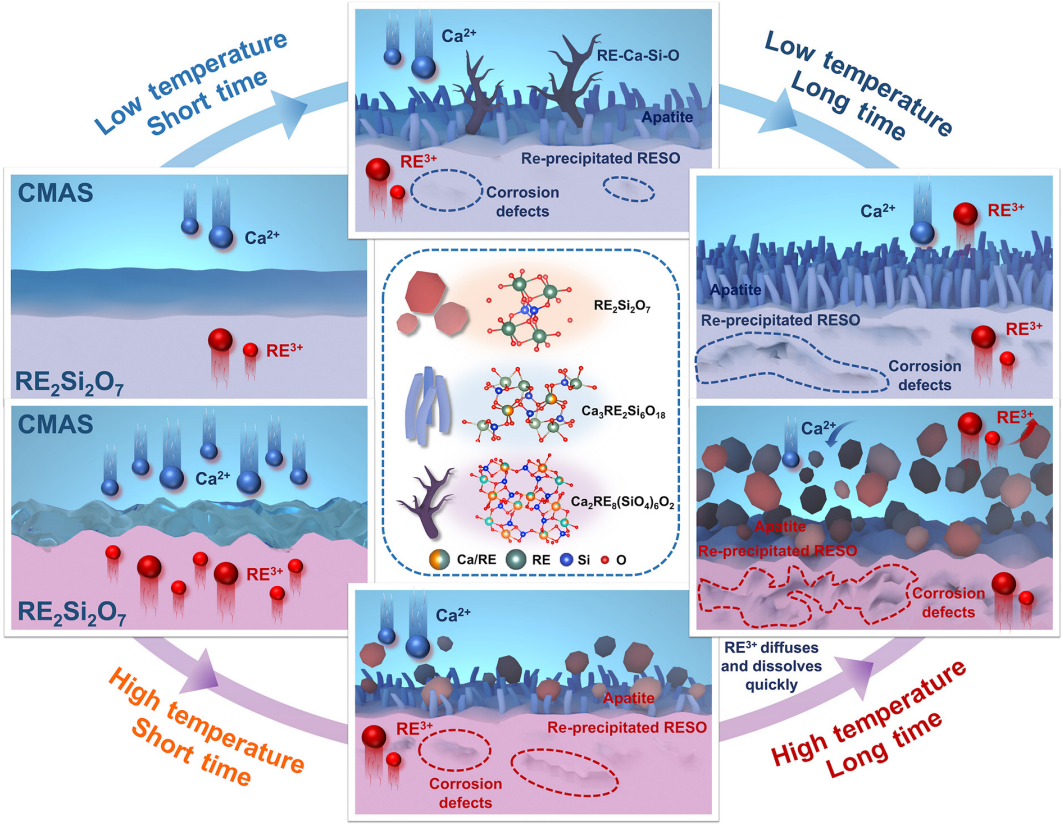

Fig. 10 Schematic diagram of corrosion mechanism of $(Er_{1/4}Y_{1/4}Lu_{1/4}Yb_{1/4})_2Si_2O_7$ and $(Er_{1/6}Tm_{1/6}Y_{1/15}Gd_{1/15}Lu_{4/15}Yb_{4/15})_2Si_2O_7$ at 1300 and 1500 °C.

enhances ion mobility, bringing the system closer to thermodynamic equilibrium. In the initial stage of corrosion, the apatite phase can still form transiently; however, with prolonged exposure, its stability decreases. Rapid consumption depletes Ca^{2+} in the CMAS melt, while the simultaneous enrichment of rare-earth elements alters the local chemistry, disrupting the original thermodynamic equilibrium and leading to the gradual dissolution of apatite. Concurrently, the delayed diffusion effect, originating from lattice distortion and chemical complexity due to rare-earth cations of varying radii, inhibits rapid elemental migration and slows phase transformation. In the later stages of corrosion, recrystallization dominates the process, eventually resulting in the reprecipitation of the rare-earth disilicate phase as the most thermodynamically stable product, which remains in the corrosion layer. In summary, temperature is a critical factor influencing the CMAS corrosion mechanism. At lower temperatures (1300 °C), kinetic factors dominate, allowing the apatite phase to remain stable. At higher temperatures (1500 °C), thermodynamic driving forces become more influential, ultimately promoting the reprecipitation of the rare-earth disilicate phase via a dissolution–reprecipitation mechanism, which persists as the final stable corrosion product.

3.4 Corrosion depth prediction based on extended Kalman filter

To expedite long-term CMAS corrosion assessment for high-entropy rare-earth silicates, an extended Kalman filter algorithm coupled with classical models is developed to accurately predict corrosion depth and rate evolution. A corrosion temperature of 1300 °C was chosen because higher temperatures (e.g., 1500 °C) may cause undesirable phase changes, thereby deviating from practical application scenarios. Next, using the 48-h corrosion depth data for the two materials at 1300 °C, we compared the error levels of several classical corrosion models. This comparison, which included the diffusion barrier and coating penetration models, provides a basis for later model integration into the EKF algorithm. Specific corrosion schemes and data are provided in Note 3 and Table S2 in the ESM. Figure 11 shows that the diffusion barrier model fits the experimental data best. For both materials, it has the smallest error (< 20%) over 48 h and shows superior linear fitting in the initial 0–24 h stage compared with other models. Therefore, the diffusion barrier model is adopted as the core kinetic framework for the subsequent EKF prediction model. From the perspective of the CMAS corrosion resistance mechanism of high-entropy rare-earth silicate materials at 1300 °C, after the sample is attacked by CMAS melt, RE^{3+} can react with Ca^{2+} in the CMAS to form a dense apatite sealing layer. Simultaneously, lattice distortion occurs in the high-entropy material, further obstructing the penetration pathways of the CMAS melt. The synergistic effect of these two factors imparts excellent corrosion resistance to the material, which is consistent with previous reports [23]. This further confirms that the diffusion barrier model accurately describes the CMAS corrosion process in high-entropy rare-earth silicates. It is therefore the best model among those tested for predicting corrosion depth in high-entropy rare-earth silicates. In practical thermal spray or physical vapor deposition (PVD) coatings, microstructural features such as porosity, microcracks, and grain boundaries influence CMAS infiltration behavior. These defects can provide preferential pathways for melt penetration, potentially accelerating corrosion progression. Our integrated EKF-diffusion barrier model effectively accounts for such microstructural influences through its parameterization of the effective diffusion coefficient and reaction rate constants. The model's capability to dynamically adjust these parameters based on experimental data enables it to capture the complex corrosion kinetics in real coating systems with inherent microstructural defects. Furthermore, the diffusion barrier model

is based on mass transport through heterogeneous media. This makes it well suited for predicting corrosion in real T/EBCs, where the microstructure creates a tortuous path for CMAS infiltration. This connection between our modeling framework and practical coating characteristics enhances the applicability of our predictive methodology to real-world T/EBC systems.

Based on the integrated framework of the diffusion barrier model and the EKF algorithm, predictions are made for the corrosion depth and corrosion rate of the two materials at different time points under 1300 °C, as shown in Figs. 12(a) and 12(b). The integration of the EKF algorithm confirmed the prediction accuracy. It reduced the relative error for the 48-h corrosion depth to below 3%, lower than the > 15% error without EKF, thereby validating the high accuracy of our models. Additionally, the distinction between this short-term validation metric and the broader methodological contribution is shown in Note 4 in the ESM.

Under the assumption of excess CMAS melt, i.e., sufficient CMAS supply during corrosion, excluding termination due to salt depletion, the corrosion rates of both materials exhibit an evolutionary characteristic of rapid decline followed by stabilization. During the initial corrosion stage (0–24 h), the thin apatite sealing layer on the material surface allows rapid CMAS melt penetration, resulting in a high corrosion rate. As the corrosion time increases, the apatite sealing layer gradually forms and densifies, increasing the resistance to CMAS penetration and reducing the corrosion rate. Beyond 48 h, the sealing layer enters a stable phase, and the corrosion rate levels off. This evolutionary trend aligns with experimental results and reported work [23,35], further confirming the accuracy of our predictions. The evolution of corrosion depth over time displays a pattern of rapid initial growth followed by deceleration. Within 0–48 h, the corrosion depth increases approximately linearly with time. After 48 h, the growth rate gradually decreases, showing a distinct saturation trend. When extended to 96 h (Figs. 12(c) and 12(d)), both materials show a stable corrosion depth of approximately 37 μm. This is lower than that of traditional YSZ, $Y_2Si_2O_7$, and $Yb_2Si_2O_7$ [42–45], confirming their excellent long-term CMAS resistance.

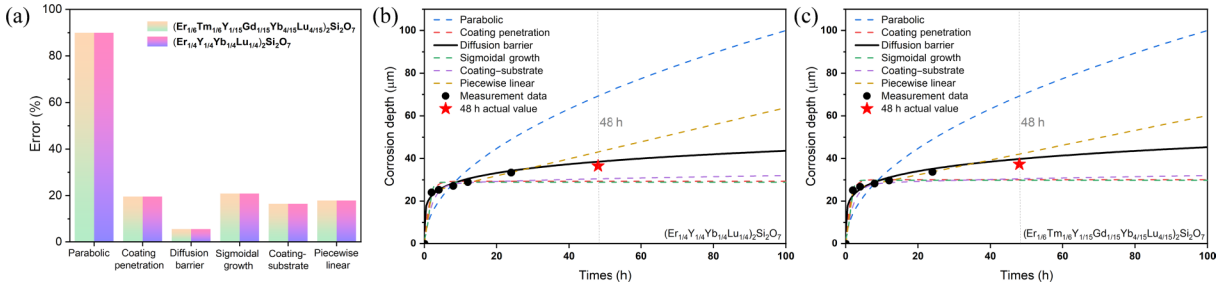

Fig. 11 (a) Error between experimental and predicted data from different classical corrosion models at 1300 °C for 48 h. Corrosion depth of experimental and predicted data after CMAS corrosion over time of (b) $(Er_{1/4}Y_{1/4}Lu_{1/4}Yb_{1/4})_2Si_2O_7$ and (c) $(Er_{1/6}Tm_{1/6}Y_{1/15}Gd_{1/15}Lu_{4/15}Yb_{4/15})_2Si_2O_7$.

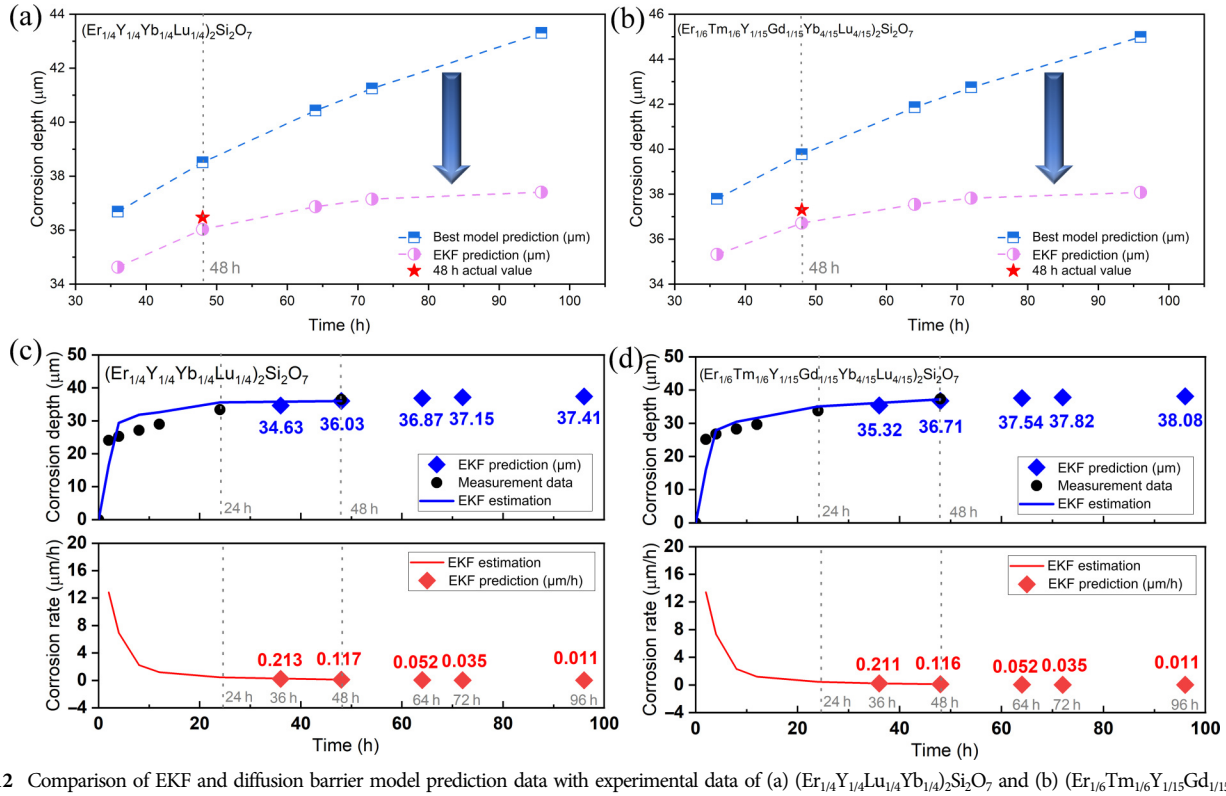

Fig. 12 Comparison of EKF and diffusion barrier model prediction data with experimental data of (a) $(Er_{1/4}Y_{1/4}Lu_{1/4}Yb_{1/4})_2Si_2O_7$ and (b) $(Er_{1/6}Tm_{1/6}Y_{1/15}Gd_{1/15}Lu_{4/15}Yb_{4/15})_2Si_2O_7$. Predicted results of corrosion depth and rate in long-term corrosive environments by EKF model for (c) $(Er_{1/4}Y_{1/4}Lu_{1/4}Yb_{1/4})_2Si_2O_7$ and (d) $(Er_{1/6}Tm_{1/6}Y_{1/15}Gd_{1/15}Lu_{4/15}Yb_{4/15})_2Si_2O_7$.

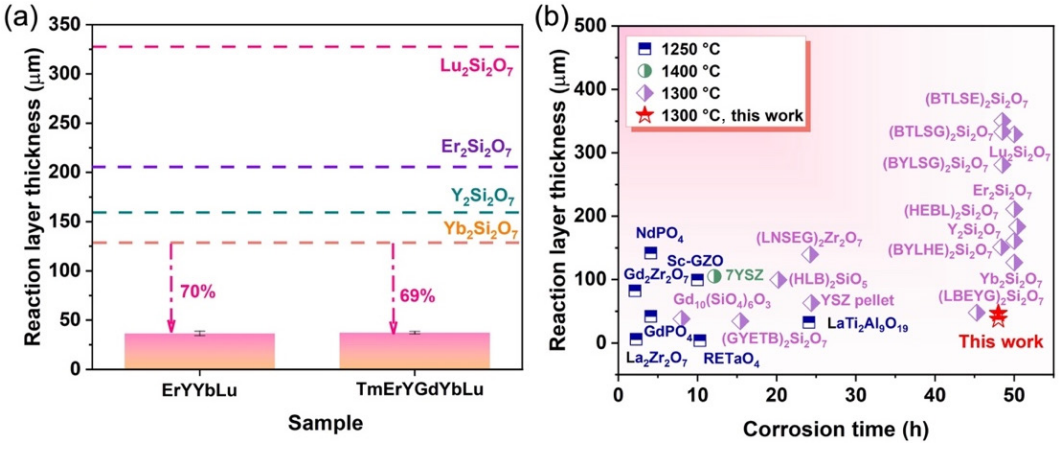

Fig. 13 (a) Corrosion depth of prepared $(nRE_{xi})_2Si_2O_7$ after CMAS corrosion and $RE_2Si_2O_7$ after CMAS corrosion at 1300 °C for approximately 48 h. (b) Summary of reported representative data on corrosion depth of several T/EBC materials in CMAS.

Table 3 Hardness values (GPa) of $(Er_{1/4}Y_{1/4}Lu_{1/4}Yb_{1/4})_2Si_2O_7$ and $(Er_{1/6}Tm_{1/6}Y_{1/15}Gd_{1/15}Lu_{4/15}Yb_{4/15})_2Si_2O_7$

Compound	0.3 kgf	0.5 kgf	1.0 kgf
$(Er_{1/4}Y_{1/4}Lu_{1/4}Yb_{1/4})_2Si_2O_7$	6.48±0.86	6.35±0.36	6.22±0.50
$(Er_{1/6}Tm_{1/6}Y_{1/15}Gd_{1/15}Lu_{4/15}Yb_{4/15})_2Si_2O_7$	6.38±0.31	6.41±0.30	5.75±0.47

4 Discussion

To validate the cocktail effect of $(Er_{1/4}Y_{1/4}Lu_{1/4}Yb_{1/4})_2Si_2O_7$ and $(Er_{1/6}Tm_{1/6}Y_{1/15}Gd_{1/15}Lu_{4/15}Yb_{4/15})_2Si_2O_7$ for their resistance to CMAS corrosion, the thicknesses of the reaction layer under similar corrosion conditions (1300 °C, 50 h) for $Yb_2Si_2O_7$, $Er_2Si_2O_7$, $Y_2Si_2O_7$, and $Lu_2Si_2O_7$ are compared, as shown in Fig. 13(a) [46]. Both materials demonstrated excellent corrosion resistance. Their reaction layer thicknesses (~36.37 and 37.3 μm) are the lowest among all samples. Even $Yb_2Si_2O_7$, which demonstrated the best corrosion resistance among the single-component materials, still has a reaction layer thickness of 125 μm—significantly higher than that of $(Er_{1/4}Y_{1/4}Lu_{1/4}Yb_{1/4})_2Si_2O_7$ and $(Er_{1/6}Tm_{1/6}Y_{1/15}Gd_{1/15}Lu_{4/15}Yb_{4/15})_2Si_2O_7$. This confirms that high-entropy design improves CMAS corrosion resistance in rare-earth disilicates. Multiprincipal element mixing creates a cocktail effect, thus boosting chemical stability and phase-structural durability in extremely high-temperature environments. Among them, the role of each RE element in improving performance is detailed in Note 5 in the ESM.

Furthermore, to evaluate the application potential of $(Er_{1/4}Y_{1/4}Lu_{1/4}Yb_{1/4})_2Si_2O_7$ and $(Er_{1/6}Tm_{1/6}Y_{1/15}Gd_{1/15}Lu_{4/15}Yb_{4/15})_2Si_2O_7$ in T/EBCs, the Vickers hardness values of $(Er_{1/4}Y_{1/4}Lu_{1/4}Yb_{1/4})_2Si_2O_7$ and $(Er_{1/6}Tm_{1/6}Y_{1/15}Gd_{1/15}Lu_{4/15}Yb_{4/15})_2Si_2O_7$ under loads of 0.3, 0.5, and 1 kgf are presented in Table 3. Both materials exhibit favorable hardness, with $(Er_{1/4}Y_{1/4}Lu_{1/4}Yb_{1/4})_2Si_2O_7$ demonstrating higher hardness than $(Er_{1/6}Tm_{1/6}Y_{1/15}Gd_{1/15}Lu_{4/15}Yb_{4/15})_2Si_2O_7$, which can be attributed to the greater distortion of $[SiO_4]$ in the former [11]. Furthermore, Fig. 13(b) summarizes the reported corrosion depth data of various T/EBC materials under CMAS corrosion conditions in recent years. The comparison shows that the prepared $(Er_{1/4}Y_{1/4}Lu_{1/4}Yb_{1/4})_2Si_2O_7$ and $(Er_{1/6}Tm_{1/6}Y_{1/15}Gd_{1/15}Lu_{4/15}Yb_{4/15})_2Si_2O_7$ exhibit excellent corrosion resistance among the compared materials [14,23,47–58]. Their outstanding resistance to CMAS corrosion is not only superior to that of common T/EBC systems but also highlights the great potential of high-entropy modification in enhancing the CMAS corrosion resistance of materials. These results demonstrate that the high-entropy design strategy can improve the applicability and service reliability of T/EBC materials in extremely high-temperature corrosive environments. Therefore, $(Er_{1/4}Y_{1/4}Lu_{1/4}Yb_{1/4})_2Si_2O_7$ and $(Er_{1/6}Tm_{1/6}Y_{1/15}Gd_{1/15}Lu_{4/15}Yb_{4/15})_2Si_2O_7$ show broad application prospects in achieving excellent corrosion resistance and provide important experimental evidence for the material design of next-generation high-performance T/EBCs.

5 Conclusions

In this study, we designed and synthesized two novel high-entropy rare-earth disilicates, $(Er_{1/4}Y_{1/4}Lu_{1/4}Yb_{1/4})_2Si_2O_7$ and $(Er_{1/6}Tm_{1/6}Y_{1/15}Gd_{1/15}Lu_{4/15}Yb_{4/15})_2Si_2O_7$. First, the developed materials demonstrate an approximately 70% reduction in corrosion depth compared with conventional single-component $RE_2Si_2O_7$, attributed to enhanced lattice distortion from multiprincipal rare-earth doping. Then, temperature-dependent corrosion mechanisms are identified. At 1300 °C, thermodynamic–kinetic competition dominates, while at 1500 °C, a dissolution–reprecipitation mechanism prevails due to accelerated ion diffusion. Last, an innovative extended Kalman filter model integrated with physical corrosion mechanisms was established, achieving accurate long-term prediction of corrosion depth and rate at 1300 °C with errors below 3%. This work provides both fundamental insights into the corrosion behavior of high-entropy disilicates and a reliable methodology for predictive lifetime assessment, advancing the development of next-generation T/EBC materials.

Acknowledgements

This work is supported by the National Natural Science Foundation of China (Nos. U21A2063, 52172071, and 51972080). Bin Liu acknowledges research support from Shanghai Technical Service Center for Advanced Ceramics Structure Design and Precision Manufacturing (No. 20DZ2294000).

Availability of data and materials

The data that support the findings of this study are available from the corresponding author upon reasonable request.

Competing interests

The authors have no competing interests to declare that are relevant to the content of this article. The authors Yuelei Bai and Bin Liu are Editorial Committee members of this journal.

Electronic Supplementary Material

Supplementary material is available in the online version of this article at https://doi.org/10.26599/JAC.2026.9221251.

References

[1] Yankova MS, Garner A, Baxter F, *et al.* Untangling competition between epitaxial strain and growth stress through examination of variations in local oxidation. *Nat Commun* 2023, **14**: 250.

[2] Chen ZY, Wang YZ, Huang YL, *et al.* Medium-entropy monosilicates deliver high corrosion resistance to calcium–magnesium aluminosilicate molten salt. *Adv Sci* 2024, **11**: 2400736.

[3] Luo YX, Sun LC, Wang JM, *et al.* Phase formation capability and compositional design of β-phase multiple rare-earth principal component disilicates. *Nat Commun* 2023, **14**: 1275.

[4] Zhang JG, Han GF, Cao XX, *et al.* Regulating the composition, structure, and nanoscale dimensions of $Yb_2Si_2O_7$ environmental barrier coating to achieve a biomimetic teakwood-like functional structure by waste gas recycling. *J Adv Ceram* 2025, **14**: 9221021.

[5] Clarke DR, Oechsner M, Padture NP. Thermal-barrier coatings for more efficient gas-turbine engines. *MRS Bull* 2012, **37**: 891–898.

[6] Sun LC, Luo YX, Tian ZL, *et al.* High temperature corrosion of $(Er_{0.25}Tm_{0.25}Yb_{0.25}Lu_{0.25})_2Si_2O_7$ environmental barrier coating material subjected to water vapor and molten calcium–magnesium–aluminosilicate (CMAS). *Corros Sci* 2020, **175**: 108881.

[7] Liu Y, Liu YW, Zhuang L, *et al.* Composition-driven superior CMAS corrosion resistance of high-entropy rare-earth disilicates. *Corros Sci* 2024, **233**: 112108.

[8] Zhou QQ, Wei YG, Xu GN, *et al.* Microstructure and microcrack evolution mechanism of thermal barrier coatings under CMAS infiltration and corrosion: Experimental and numerical modeling. *Corros Sci* 2024, **229**: 111890.

[9] Sun Y, Nie XX, Cai CY, *et al.* Phase transformation failure in YSZ TBCs induced by component-dependent CMAS corrosion. *Surf Coat Tech* 2023, **464**: 129547.

[10] Yan G, Liu W, Sun Y, *et al.* Failure behavior of $RE_2M_2O_7$/YSZ TBCs prepared by EB-PVD in gas thermal shock-CMAS corrosion environment. *J Eur Ceram Soc* 2025, **45**: 117027.

[11] Tan ZY, Yang ZH, Zhu W, *et al.* Mechanical properties and calcium–magnesium–alumino–silicate (CMAS) corrosion behavior of a promising $Hf_6Ta_2O_{17}$ ceramic for thermal barrier coatings. *Ceram Int* 2020, **46**: 25242–25248.

[12] Hao SQ, Oleksak RP, Doğan ÖN, *et al.* Computational design of high-entropy rare earth disilicates as next-generation thermal/environmental barrier coatings. *Acta Mater* 2023, **258**: 119225.

[13] Chen GH, Zhang YL, Guo XT, *et al.* Microstructure and water corrosion behavior of $(Lu_{0.2}Yb_{0.2}Er_{0.2}Tm_{0.2}Sc_{0.2})_2Si_2O_7$ high-entropy rare-earth disilicate coating for SiC coated C/C composites. *J Eur Ceram Soc* 2023, **43**: 3647–3657.

[14] Wang X, Meng MY, Xu FH, *et al.* $(Lu_{1/7}Yb_{1/7}Sc_{1/7}Er_{1/7}Y_{1/7}Ho_{1/7}Dy_{1/7})_2Si_2O_7$ high entropy rare-earth disilicate with low thermal conductivity and excellent resistance to CMAS corrosion. *J Adv Ceram* 2024, **13**: 549–560.

[15] Cao L, Zhang QQ, Du LJ, *et al.* Synthesis and characterization of high entropy $(TiVNbTaM)_2AlC$ (M = Zr, Hf) ceramics. *J Adv Ceram* 2024, **13**: 237–246.

[16] Cai FY, Ni DW, Dong SM. Research progress of high-entropy carbide ultra-high temperature ceramics. *J Inorg Mater* 2024, **39**: 591.

[17] Nie XD, Xu JY, Zhang ZC, *et al.* The progress of research on high-entropy ceramics in the field of tribology. *Adv Ceram* 2025, **46**: 1–23.

[18] Fan Y, Bai YL, Li Q, *et al.* Compositional design and phase formation capability of high-entropy rare-earth disilicates from machine learning and decision fusion. *npj Comput Mater* 2024, **10**: 95.

[19] Wang X, Cheng MH, Xiao GZ, *et al.* Preparation and corrosion resistance of high-entropy disilicate $(Y_{0.25}Yb_{0.25}Er_{0.25}Sc_{0.25})_2Si_2O_7$ ceramics. *Corros Sci* 2021, **192**: 109786

[20] Poerschke DL, Shaw JH, Verma N, *et al.* Interaction of yttrium disilicate environmental barrier coatings with calcium–magnesium–iron alumino–silicate melts. *Acta Mater* 2018, **145**: 451–461.

[21] Krämer S, Yang J, Levi CG. Infiltration-inhibiting reaction of gadolinium zirconate thermal barrier coatings with CMAS melts. *J Am Ceram Soc* 2008, **91**: 576–583.

[22] Ahlborg NL, Zhu DM. Calcium–magnesium aluminosilicate (CMAS) reactions and degradation mechanisms of advanced environmental barrier coatings. *Surf Coat Tech* 2013, **237**: 79–87.

[23] Dong Y, Ren K, Wang QK, *et al.* Interaction of multicomponent disilicate $(Yb_{0.2}Y_{0.2}Lu_{0.2}Sc_{0.2}Gd_{0.2})_2Si_2O_7$ with molten calcia–magnesia–aluminosilicate. *J Adv Ceram* 2022, **11**: 66–74.

[24] Wen T, Wang JC, Cai BG, *et al.* A dynamic estimation method for the headway of virtual coupling trains utilizing the high-order extended Kalman filter-based smoother. *IEEE T Intell Transp* 2025, **26**: 7051–7064.

[25] Guo Y, Pang QH, Yin XL, *et al.* Bayesian adaptive extended Kalman-based orbit determination for optical observation satellites. *Sensors* 2025, **25**: 2527.

[26] Fan Y, Bai YL, Lu ZY, *et al.* Unlocking compositional design and mechanism for mechanical/thermal properties of high-entropy rare-earth disilicates. *J Am Ceram Soc* 2026, **109**: 70388.

[27] Zhai HN, Liu HB, Zhang YF, *et al.* Freestanding 1T MoS_2@MXene hybrid film with strong interfacial interaction for highly reversible zinc ions storage. *J Mater Sci Technol* 2024, **188**: 183–190.

[28] Yu TT, Yang B, Zhang R, *et al.* Fabrication of a novel Z–S-scheme photocatalytic fuel cell with the Z-scheme TiO_2/GO/g-C_3N_4 photoanode and S-scheme $BiOAc_{1-x}Br_x$/BiOBr photocathode for TC degradation. *J Mater Sci Technol* 2024, **188**: 11–26.

[29] Zhao SJ, Stocks GM, Zhang YW. Stacking fault energies of face-centered cubic concentrated solid solution alloys. *Acta Mater* 2017, **134**: 334–345.

[30] Liu YC, Jia DC, Zhou Y, *et al.* $Zn_{0.1}Ca_{0.1}Sr_{0.4}Ba_{0.4}ZrO_3$: A non-equimolar multicomponent perovskite ceramic with low thermal conductivity. *J Eur Ceram Soc* 2020, **40**: 6272–6277.

[31] Kamalan Kirubaharan AM, Kuppusami P, Priya R, *et al.* Synthesis, microstructure and corrosion behavior of compositionally graded Ni–YSZ diffusion barrier coatings on inconel-690 for applications in high temperature environments. *Corros Sci* 2018, **135**: 243–254.

[32] Van Nguyen T, Hubbard JB, Pommersheim JM. Unified model for the degradation of organic coatings on steel in a neutral electrolyte. *J Coating Technol* 1996, **68**: 45–56.

[33] Tian ZL, Zheng LY, Wang JM, *et al.* Damage tolerance and extensive plastic deformation of β-$Yb_2Si_2O_7$ from room to high temperatures. *J Am Ceram Soc* 2015, **98**: 2843–2851.

[34] Meng H, Wei P, Tang ZY, *et al.* Data-driven discovery of formation ability descriptors for high-entropy rare-earth monosilicates. *J Materiomics* 2024, **10**: 738–747.

[35] Xiao GZ, Shen QY, Tian Y, *et al.* Investigation on the relation of microstructures and CMAS corrosion resistance of high entropy RE disilicates. *Corros Sci* 2024, **227**: 111727.

[36] Li JX, Li LY, Wang PC, *et al.* Regulation in CMAS corrosion behavior of high entropy RE monosilicates by component design of doped RE. *Ceram Int* 2025, **51**: 17828–17836.

[37] Liu XY, Zhang P, Huang MZ, *et al.* Effect of lattice distortion in high-entropy $RE_2Si_2O_7$ and RE_2SiO_5 (RE = Ho, Er, Y, Yb, and Sc) on their thermal conductivity: Experimental and molecular dynamic simulation study. *J Eur Ceram Soc* 2023, **43**: 6407–6415.

[38] Duffy JA, Ingram MD. An interpretation of glass chemistry in terms of the optical basicity concept. *J Non-Cryst Solids* 1976, **21**: 373–410.

[39] Wolf M, Mack DE, Guillon O, *et al.* Resistance of pure and mixed rare earth silicates against calcium–magnesium–aluminosilicate (CMAS): A comparative study. *J Am Ceram Soc* 2020, **103**: 7056–7071.

[40] Tian ZL, Zhang J, Zhang TY, *et al.* Towards thermal barrier coating application for rare earth silicates RE_2SiO_5 (RE = La, Nd, Sm, Eu, and Gd). *J Eur Ceram Soc* 2019, **39**: 1463–1476.
[41] Schulz U, Braue W. Degradation of $La_2Zr_2O_7$ and other novel EB-PVD thermal barrier coatings by CMAS (CaO–MgO–Al_2O_3–SiO_2) and volcanic ash deposits. *Surf Coat Tech* 2013, **235**: 165–173.
[42] Zhang CG, Fan Y, Zhao JL, *et al.* Corrosion resistance of nonstoichiometric gadolinium zirconate coatings against CaO–MgO–Al_2O_3–SiO_2 silicate. *J Eur Ceram Soc* 2021, **41**: 3687–3695.
[43] Zhang CG, Fan Y, Zhao JL, *et al.* Corrosion resistance of non-stoichiometric gadolinium zirconate fabricated by laser-enhanced chemical vapor deposition. *J Adv Ceram* 2021, **10**: 520–528.
[44] Zhao HB, Richards BT, Levi CG, *et al.* Molten silicate reactions with plasma sprayed ytterbium silicate coatings. *Surf Coat Tech* 2016, **288**: 151–162.
[45] Summers WD, Poerschke DL, Park D, *et al.* Roles of composition and temperature in silicate deposit-induced recession of yttrium disilicate. *Acta Mater* 2018, **160**: 34–46.
[46] Yeh JW, Chen SK, Lin SJ, *et al.* Nanostructured high-entropy alloys with multiple principal elements: Novel alloy design concepts and outcomes. *Adv Eng Mater* 2004, **6**: 299–303.
[47] Tian ZL, Ren XM, Lei YM, *et al.* Corrosion of $RE_2Si_2O_7$ (RE = Y, Yb, and Lu) environmental barrier coating materials by molten calcium–magnesium–alumino–silicate glass at high temperatures. *J Eur Ceram Soc* 2019, **39**: 4245–4254.
[48] Ma WY, Luo YB, Ma Z, *et al.* $La_2Zr_2O_7$ based high entropy ceramic with a low thermal conductivity and enhanced CMAS corrosion resistance. *Ceram Int* 2023, **49**: 29729–29735.
[49] Wang F, Guo L, Wang CM, *et al.* Calcium–magnesium–alumina–silicate (CMAS) resistance characteristics of $LnPO_4$ (Ln = Nd, Sm, Gd) thermal barrier oxides. *J Eur Ceram Soc* 2017, **37**: 289–296.
[50] Li DX, Jiang P, Gao RH, *et al.* Experimental and numerical investigation on the thermal and mechanical behaviours of thermal barrier coatings exposed to CMAS corrosion. *J Adv Ceram* 2021, **10**: 551–564.
[51] Li BW, Sun JY, Guo L. CMAS corrosion behavior of Sc doped $Gd_2Zr_2O_7$/YSZ thermal barrier coatings and their corrosion resistance mechanisms. *Corros Sci* 2021, **193**: 109899.
[52] Wu D, Zhang H, Shan X, *et al.* A novel CMAS-resistant material based on thermodynamic equilibrium design: Apatite-type $Gd_{10}(SiO_4)_6O_3$. *J Am Ceram Soc* 2020, **103**: 3401–3415.
[53] Tu TZ, Liu JX, Zhou L, *et al.* Graceful behavior during CMAS corrosion of a high-entropy rare-earth zirconate for thermal barrier coating material. *J Eur Ceram Soc* 2022, **42**: 649–657.
[54] Chen ZL, Tian ZL, Zheng LY, *et al.* Thermo-mechanical properties and CMAS resistance of $(Ho_{0.4}Yb_{0.3}Lu_{0.3})_2SiO_5$ solid solution for environmental barrier coating applications. *Ceram Int* 2023, **49**: 6429–6439.
[55] Qu WW, Li SS, Chen ZH, *et al.* Hot corrosion behavior and wettability of calcium–magnesium–alumina–silicate (CMAS) on $LaTi_2Al_9O_{19}$ ceramic. *Corros Sci* 2020, **162**: 108199.
[56] Bryce K, Shih YT, Huang LP, *et al.* Calcium–magnesium–aluminosilicate (CMAS) corrosion resistance of high entropy rare-earth phosphate $(Lu_{0.2}Yb_{0.2}Er_{0.2}Y_{0.2}Gd_{0.2})PO_4$: A novel environmental barrier coating candidate. *J Eur Ceram Soc* 2023, **43**: 6461–6472.
[57] Chen ZL, Tian ZL, Zheng LY, *et al.* $(Ho_{0.25}Lu_{0.25}Yb_{0.25}Eu_{0.25})_2SiO_5$ high-entropy ceramic with low thermal conductivity, tunable thermal expansion coefficient, and excellent resistance to CMAS corrosion. *J Adv Ceram* 2022, **11**: 1279–1293.
[58] Li H, Yu YP, Fang B, *et al.* Calcium–magnesium–alumina–silicate (CMAS) corrosion behavior of $A_6B_2O_{17}$ (A = Zr, Hf; B = Nb, Ta) as potential candidate for thermal barrier coating (TBC). *Corros Sci* 2022, **204**: 110395.